Mineral weathering and bedrock weakening: Modeling microscale bedrock damage under biotite weathering

Xianda Shen[1], Chloe Arson[1], Ken L. Ferrier[2], Nicole West[3], Sheng Dai[1]

[1]School of Civil and Environmental Engineering, Georgia Institute of Technology
[2]Department of Geoscience, University of Wisconsin Madison
[3]Department of Earth and Atmospheric Sciences, Central Michigan University

Key Points:

- We present a new model for the effects of mineral chemical weathering on the evolution of microscale bedrock damage
- We apply the model to the expansion of biotite during chemical weathering
- Damage is affected by biotite abundance, aspect ratio, and orientation
- This provides a foundation for dynamic models of macroscale fracture development

Corresponding author: =name=, `=email address=`

Abstract

Bedrock weakening is of wide interest because it influences landscape evolution, chemical weathering, and subsurface hydrology. A longstanding hypothesis states that bedrock weakening is driven by chemical weathering of minerals like biotite, which expand as they weather and create stresses sufficient to fracture rock. Here we build on recent advances in rock damage mechanics to develop a model for the influence of multi-mineral chemical weathering on bedrock damage, which is defined as the reduction in bedrock stiffness. We use biotite chemical weathering as an example application of this model to explore how the abundance, aspect ratio, and orientation affect the time-dependent evolution of bedrock damage during biotite chemical weathering. Our simulations suggest that biotite abundance and aspect ratio have a profound effect on the evolution of bedrock damage during biotite chemical weathering. These characteristics exert particularly strong influences on the timing of the onset of damage, which occurs earlier under higher biotite abundances and smaller biotite aspect ratios. Biotite orientation, by contrast, exerts a relatively weak influence on damage. Our simulations further show that damage development is strongly influenced by the boundary conditions, with damage initiating earlier under laterally confined boundaries than under unconfined boundaries. These simulations suggest that relatively minor differences in biotite populations can drive significant differences in the progression of rock weakening. This highlights the need for observations of biotite abundance, aspect ratio, and orientation at the mineral and field scales, and motivates efforts to upscale this microscale model to investigate the evolution of the macroscale fracture network.

1 Introduction

Many weathering profiles contain a layer of fractured, chemically weathered material between bedrock and soil that retains much of the character of the parent bedrock. This layer is variously referred to as saprolite, saprock, or weathered rock (e.g., S. P. Anderson, Dietrich, & Brimhall Jr, 2002, Buss et al., 2017), and for simplicity in this study we refer to it as saprolite. Understanding the controls on this layer is of wide interest because of its role in landscape evolution (e.g., Dixon, Heimsath, & Amundson, 2009), nutrient supply (e.g., Shiels & Walker, 2003), landslide hazards (e.g., Lacerda, 2007), and the global carbon cycle (Berner, Lasaga, & Garrels, 1983; Walker, Hays, & Kasting, 1981).

A leading hypothesis posits that saprolite production is dominantly controlled by chemical weathering of Fe-bearing minerals, which expand as they weather and create stresses sufficient to strain and weaken rock under certain mineralogical conditions. Previous studies have investigated this hypothesis using models to compute fracture size from the strain energy generated by mineral expansion, which provide an important constraint on the net change in fracture size after weathering (Buss, Sak, Webb, & Brantley, 2008; Fletcher, Buss, & Brantley, 2006; Goodfellow et al., 2016; A. Navarre-Sitchler, Brantley, & Rother, 2015; A. Navarre-Sitchler, Steefel, Sak, & Brantley, 2011; A. K. Navarre-Sitchler et al., 2013; Reis & Brantley, 2017). To date, however, no model has been developed for the transient weakening of bedrock under a continually evolving mineral chemical weathering field, which limits our ability to understand the coevolution of chemical weathering and bedrock weakening.

Following the conventional usage of the term "damage" in continuum mechanics (e.g., Houlsby & Puzrin, 2007; Lemaitre & Desmorat, 2005; Yu, 2007), in this study we define damage Ω as a scalar that quantifies the reduction in a rock's stiffness from its initial reference stiffness. For example, at $\Omega = 0$ (no damage), the rock has its reference stiffness. At $\Omega > 0$, the rock has a stiffness smaller than its reference value. This definition of damage is analogous to some commonly used terms for changes in the me-

chanical character of rock, but it differs from them in some important ways. For example, damage differs from the volumetric concentration of micro-cracks, which, unlike the damage variable used in our model, is not necessarily linearly related to changes in rock stiffness (e.g., Budiansky & O'connell, 1976; Germanovich, Salganik, Dyskin, & Lee, 1994). It is also distinct from mechanical weathering, a term that encompasses all processes that drive near-surface rock fracturing, such as freeze-thaw cycling, solar heating, crystal growth, root expansion, and erosional unloading (e.g., Eppes & Keanini, 2017; McFadden, Eppes, Gillespie, & Hallet, 2005). In this study, we use the term damage rather than mechanical weathering because in our model, damage quantifies the loss of elastic deformation energy, and, by proxy, the loss of stiffness (Section 2).

In the past few years, advances in rock damage theory have improved our understanding of the damage done by mineral chemical weathering. At the same time, advances in numerical modeling have improved the implementation of chemo-mechanical damage processes in coupled thermodynamic models. For example, recently developed hydro-chemo-mechanical models have been used to predict damage in sandstones (Hu et al., 2012) and rock pillars (Li, Tang, Wang, & Yu, 2013). Similarly, new thermodynamic models have successfully captured the dissolution of iron-bearing minerals to study the mechanical stability of abandoned mines (Grgic, Giraud, & Auvray, 2013; Poulet, Karrech, Regenauer-Lieb, Fisher, & Schaubs, 2012). An analogous model was applied to explain the reduction of fracture aperture in granites subject to hydrothermal dissolution and precipitation (Yasuhara et al., 2011). Subcritical cracking, the primary bond-breaking process for the near surface rock (Eppes & Keanini, 2017), and brittle creep models have been successfully used to predict delayed failure in a variety of lithologies (Brantut, Baud, Heap, & Meredith, 2012; Brantut, Heap, Meredith, & Baud, 2013; Stefanou & Sulem, 2014) and to simulate borehole spalling and breakout (Schoenball, Sahara, & Kohl, 2014). So far, however, no model accounts for both the effects of chemical reactions on rock stiffness and strength and the effects of fracturing on chemical weathering. The model proposed in this paper provides a first step toward overcoming this limitation.

Here we develop a new model to explore the influence of mineral chemical weathering on bedrock damage. The model begins with a model of mineral deformation at the crystal scale (Section 2.1) and builds up to a model for the transient evolution of damage at the scale of a Representative Elementary Volume, or REV. To illustrate the behavior of the model, we apply the model to chemical weathering of biotite (Section 2.4). Biotite is abundant in many igneous and metamorphic rocks (e.g., Bateman, 1992) and undergoes exceptionally large expansion during weathering (e.g., Banfield & Eggleton, 1988). Biotite's role in fracturing rock has been the subject of considerable attention in previous studies (e.g., Buss et al., 2008; Fletcher et al., 2006; Goodfellow et al., 2016; Wahrhaftig, 1965; White et al., 2002) because it expands more during weathering than other primary minerals do, and therefore provides an upper bound on the extent to which chemical weathering of a single mineral phase is capable of driving rock fracture. We use this model to explore how biotite characteristics influence the evolution of the rock's mechanical characteristics. Our simulations show that the development of bedrock damage can be strongly influenced by biotite abundance, aspect ratio, and orientation, supporting the hypothesis that biotite chemical weathering can be a significant driver of bedrock damage.

2 A chemo-mechanical model of bedrock strain and damage at the REV scale

Here we formulate a 3D model for the influence of multi-mineral chemical weathering on strain and damage in a bedrock REV, which is ∼100-1,000 times larger by length than the modeled mineral. We represent the bedrock as a multi-phase material consisting of ellipsoidal mineral inclusions embedded in a homogeneous matrix. The matrix behavior is governed by a Continuum Damage Mechanics (CDM) model (Section 2.2). In-

clusions are represented by ellipsoids, which facilitates homogenization at the REV scale (Section 2.3).

2.1 A crystal-scale model of mineral deformation

We begin the crystal-scale model of mineral deformation by representing mineral crystals as oblate spheroids. This assumed shape allows us to capture several essential characteristics of mineral chemical weathering and bedrock damage. In the theory of homogenization, phases with different stiffness can be represented as inclusions and the matrix, as a homogeneous medium around those inclusions. If the inclusions are ellipsoidal, then the state of stress and strain in each inclusion and in the matrix is uniform, and all phases are homogeneous (Eshelby, 1957). Thus, the adoption of an ellipsoidal shape for all inclusions permits us to develop an analytical closed formulation based on Eshelby's scheme (Eshelby, 1957) to calculate the spatial and temporal evolution of the rock's strain, stress, and damage fields. This would not be possible if the minerals were represented as rectangular prisms, which would have nonuniform stress and strain fields.

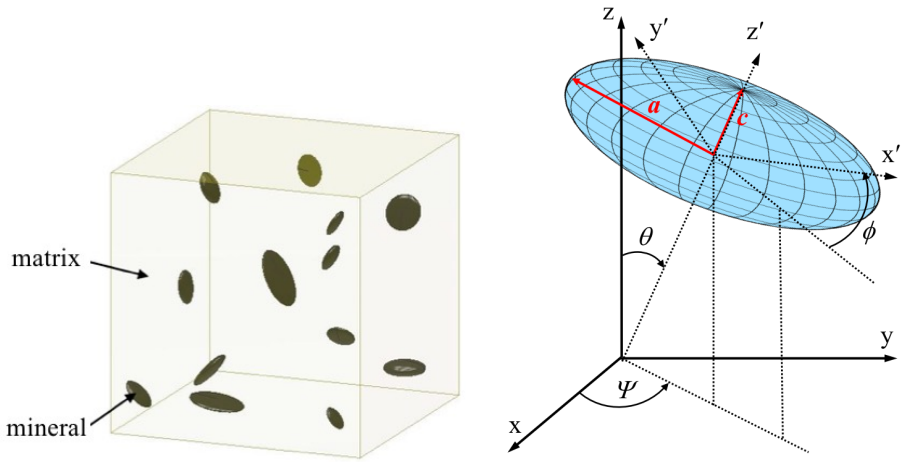

(a) Schematic of the REV (b) Schematic of the inclusion

Figure 1. Schematic of the crystal-scale weathering model.

Schematic representations of the mineral inclusion and of the REV are shown in Figure 1. We define a and c to be the long and short axes of the spheroidal mineral inclusions, respectively. Note that these definitions of a and c are not the same as the crystallographic a and c axes, which are not directly relevant for our model. During weathering, the modeled mineral inclusions remain oblate spheroids, but their aspect ratio a/c changes over time due to chemically-driven deformation in either a or c direction. Note that the proposed model can account for inclusions strains that are either positive (expansion, e.g., by hydration) or negative (shrinkage, e.g., due to mass loss). Here, we present a general modeling framework that does not require making any assumption on the type of mineral represented by the inclusions, nor on the sign of the chemically-induced strain.

For notational clarity, we distinguish between the chemically-driven strain, which is directly generated by inclusions' chemical strains, and the total strain, which is the combination of chemically-driven strain and additional strain induced by the mechanical responses of the matrix and the inclusions. We denote the chemical strain with the superscript c and a subscript indicating the direction of strain (e.g., ϵ_a^c and ϵ_c^c), and we denote the total strain by a single subscript indicating the direction of strain (e.g., ϵ_a and ϵ_c).

We assume that weathered and unweathered mineral crystals are linear elastic materials, and that inelastic effects are accounted for via the chemical strain of the inclusion. We consider that the inclusions have an isotropic mechanical behavior, by analogy to the mechanical behavior of salt crystals and amorphous solid crystals such as quartz (Bosworth, 1981; Guéry, Cormery, Shao, & Kondo, 2008; Shen & Arson, 2019). For times in which a mineral crystal is partially weathered, we calculate the elastic moduli of the partially weathered inclusion as the volumetric average of the moduli of the unweathered part of the inclusion (which has a volume of $V_{mineral}$) and of the moduli of the weathered part of the inclusion (which has a volume of $V^{w}_{mineral}$). This approximation assumes that the subscale strain field is uniform.

2.2 Damage model for the matrix

Mineral chemical weathering induces inclusions' chemical eigenstrains. Inclusions are embedded in a rock matrix constrained by far field stresses. The accumulation of chemical eigenstrains in the inclusions results in stress concentrations in the rock matrix around them. If the latter exceeds the strength of the matrix, micro-cracks initiate and the stiffness and strength of the matrix decrease. We model micro-crack propagation with a CDM model, in which the damage variable (the scalar Ω) allows quantifying weakening via a decrease of stiffness.

Within the CDM framework, the Legendre transform of the internal energy in reference to temperature, called Helmholtz free energy, is a function of damage (Houlsby & Puzrin, 2007). The Helmholtz matrix free energy is important because it influences the force that induces damage (Voyiadjis & Kattan, 2005). To ensure the symmetry and positivity of the damaged stiffness tensor, and to ensure that the non-damaged behavior of the matrix is linear elastic, we express the matrix Helmholtz free energy Ψ_s as (Halm & Dragon, 1998):

$$\Psi_s = \frac{1}{2}\lambda(\mathrm{tr}\epsilon_m)^2 + \mu\mathrm{tr}(\epsilon_m \cdot \epsilon_m) + \alpha\mathrm{tr}(\epsilon_m)\mathrm{tr}(\Omega\epsilon_m) + 2\beta\mathrm{tr}(\Omega\epsilon_m \cdot \epsilon_m) \tag{1}$$

where λ and μ are the Lamé constants of the non-damaged matrix, α and β are damage constitutive parameters and ϵ_m refers to the strain field in the matrix. α and β control the effects of damage on the reduction of λ and μ respectively. In our CDM approach, damage occurs when a damage criterion f_d exceeds a critical value. The damage criterion depends on both the so-called damage driving force, Y_d, and the damage itself (Houlsby & Puzrin, 2007; Lemaitre & Desmorat, 2005; Yu, 2007). This captures the observation that more energy is required to induce new damage in a more damaged rock than a less damaged rock (Halm & Dragon, 2002):

$$f_d = \frac{Y_d}{\sqrt{2}} - (k_0 + k_1\Omega) \tag{2}$$

where k_o is the damage initiation threshold and k_1 is a damage hardening parameter. The damage driving force Y_d is calculated from thermodynamic conjugation relationships, as follows:

$$Y_d = -\frac{\partial\Psi_s}{\partial\Omega} = -\alpha\mathrm{tr}(\epsilon_m)\mathrm{tr}(\epsilon_m) - 2\beta\mathrm{tr}(\epsilon_m \cdot \epsilon_m) \tag{3}$$

During the initiation and propagation of damage, the consistency conditions hold (i.e., the state of stress is on the elastic/damage boundary, and stays there: $\dot{f}_d = 0$ and $f_d = 0$), which allows calculating the damage rate as follows:

$$\begin{aligned} \frac{d\Omega}{dt} &= 0 && \text{if } f_d < 0 \\ \frac{d\Omega}{dt} &= \frac{1}{k_1\sqrt{2}}\frac{dY_d}{dt} && \text{if } f_d = 0 \end{aligned} \tag{4}$$

2.3 A homogenization scheme for bedrock strain and damage at the REV scale

The last component of the rock damage model is designed to compute the evolution of the bedrock REV stiffness tensor over time. For this, we adopt a Mori-Tanaka homogenization scheme (Mori & Tanaka, 1973), in which the stiffness tensor of the REV is deduced from a set of equations that relate the stress and strain fields at the REV scale to those defined in the inclusions and in the surrounding matrix. The mechanical interactions between the inclusions is accounted for via the matrix. In our application of the Mori-Tanaka homogenization scheme, each mineral inclusion is assigned an aspect ratio and an orientation θ relative to horizontal, and is embedded in a solid matrix of infinite extent (Figure 1).

The REV consists of j phases: j-1 mineral phases and one matrix phase. A collection of mineral inclusions that have identical mechanical and chemical properties in the initial (reference) state is represented as one phase. Each phase may contain an infinite number of inclusion orientations and aspect ratios. To describe the groups of inclusions in the same phase that share the same aspect ratio and orientation, we introduce the term "inclusion set". We apply the term "component" to each constituent in the REV. In this terminology, the matrix is one component, each mineral inclusion set is a component, and together all components constitute the entirety of the REV.

The homogenization scheme is based on Eshelby's theory, which proves that the state of stress in each ellipsoidal inclusion is uniform (Eshelby, 1957). In the i-th component, the local stress σ_i is expressed as a function of the local strain ϵ_i and of the local eigenstrain ϵ_i^c (i.e. the strain field that would exist in each phase in the absence of the other phases around them; here, chemical weathering strain) (Pichler & Hellmich, 2010):

$$\sigma_i = \mathbf{C}_i : \epsilon_i - \mathbf{C}_i : \epsilon_i^c \tag{5}$$

where $\mathbf{C}_i$ is the fourth-order stiffness tensor of the i-th component, and σ_i and ϵ_i are all second-order tensors.

Due to strain compatibility and stress admissibility, the macroscopic strain $\bar{\epsilon}$ (respectively, the macroscopic stress $\bar{\sigma}$) is the volume average of the local strains ϵ_i (respectively, the volume average of the local stresses σ_i) in all components over the REV. Concentration tensors operators are introduced. The concentration tensor $\mathbf{A}_i$ transforms a REV-scale strain field into its microscopic counterpart in the ith component. The homogenized stiffness $\mathbf{C}_{hom}$ of the REV is the volume average of the stiffness of all components $\mathbf{C}_i$ multiplied by the component-specific concentration tensor :

$$\mathbf{C}_{hom} = \sum_{i=1}^{n} \phi_i \mathbf{C}_i : \mathbf{A}_i \tag{6}$$

where n is the number of components in the REV (i.e., the number of biotite inclusion sets plus one, for the matrix) and ϕ_i is the volume fraction of component i.

Based on Eshelby's theory, the state of stress in each biotite inclusion is assumed uniform and the concentration tensor $\mathbf{A}_i$ can be calculated as follows (Hill, 1965):

$$\mathbf{A}_i = \mathbf{A}_i^o : \left(\sum_{j=1}^{n} \phi_i \mathbf{A}_i^o \right)^{-1} \tag{7}$$

in which:

$$\mathbf{A}_i^o = [\mathbf{I} + \mathbf{P}_i : (\mathbf{C}_i - \mathbf{C}_o)]^{-1} \tag{8}$$

In the Mori-Tanaka scheme, the stiffness of the infinite medium $\mathbf{C}_o$ is equal to the matrix stiffness (which depends on damage Ω in the present model). $\mathbf{P}_i$ is a fourth-order

tensor specific to each inclusion. The full expression of $\mathbf{P}_i$, given in Mura (1987), depends on the orientation and aspect ratio of the ellipsoidal inclusions of component i as well as on the matrix stiffness $\mathbf{C}_o$.

According to Levin's theorem (Levin, 1967), the REV stress $\bar{\sigma}$ is expressed as a function of the REV strain $\bar{\epsilon}$ and of the eigenstrain of each component, as follows:

$$\bar{\sigma} = \mathbf{C}_{hom} : \bar{\epsilon} - \sum_{i=1}^{n} \phi_i \mathbf{C}_i : \epsilon_i^c : \mathbf{A}_i \tag{9}$$

On the right side of Equation 9, the first term ($\mathbf{C}_{hom} : \bar{\epsilon}$) is the linear elasticity relation for a homogeneous medium, while the second term describes how the REV stress is modified by the eigenstrain of each component in the REV.

The strain field in each component (noted ϵ_i) is related to the macroscopic strain field and to the eigenstrains of that component, as follows:

$$\epsilon_i = \mathbf{A}_i : \bar{\epsilon} + \sum_{j=1}^{n} \mathbf{D}_{ij} \epsilon_j^c \tag{10}$$

where $\mathbf{D}_{ij}$ is the influence tensor, which accounts for the influence of a component's eigenstrain on other components (Pichler & Hellmich, 2010).

Substituting Eq.10 into Eq.5, using stress admissibility conditions and comparing with Eq. 9, the expression of $\mathbf{D}_{ij}$ is given by Pichler and Hellmich (2010), as follows:

$$\mathbf{D}_{ij} = \Bigg\{ \delta_{ij} \mathbf{A}_i^o : \mathbf{P}_i - \phi_j \mathbf{A}_i : \mathbf{A}_j^o : \mathbf{P}_j + \left[\mathbf{A}_i : \overline{\mathbf{A}^o : \mathbf{P}} - \mathbf{A}_i^o : \mathbf{P}_i \right] : \left[\overline{(\mathbf{C}_{hom} - \mathbf{C}) : \mathbf{A}^o : \mathbf{P}} \right]^{-1} : \phi_j \left[(\mathbf{I} - \mathbf{A}_j)^T + (\mathbf{C}_{hom} - \mathbf{C}_j) : \mathbf{A}_j^o : \mathbf{P}_j) \right] \Bigg\} : \mathbf{C}_j \tag{11}$$

where δ_{ij} is the Kronecker delta.

To summarize, the model developed in Sections 2.1-2.3 allows calculating the transient evolution of microscopic damage in bedrock. This is driven by the deformation of mineral inclusions during the chemical weathering of minerals. This chemical deformation, called eigenstrain, changes the states of stress and strain in the matrix, which in turn influence the state of stress in the mineral inclusions. These stress and strain changes are used to predict the initiation and propagation of damage when the matrix strains (which are related to the matrix damage driving force) exceed the threshold $\sqrt{2}\,(k_0 + k_1\Omega)$ in Equation 2. The resolution algorithm for solving these equations is detailed in Appendix A. The proposed model can be used to investigate the effects of multi-mineral chemical weathering on the evolution of bedrock damage.

2.4 Model application: biotite weathering in bedrock

As an illustration, we apply the model to a single mineral phase that experiences exceptionally large expansion during chemical weathering: biotite. In order to predict the strain and mechanical damage of bedrock due to the chemical weathering of biotite, we begin with a parameterization for biotite chemical weathering at the crystal scale (∼0.1-1 mm).

Biotite is an easily weathered sheet silicate that can undergo a number of transformations from unweathered biotite to altered biotite to 2:1 clays (e.g., vermiculite and smectite) to 1:1 clays (e.g., kaolinite and halloysite), depending on the intensity of the weathering environment (Ahn & Peacor, 1987; Buss et al., 2008; Dong, Peacor, & Murphy, 1998; Fanning, Keramidas, & El-Desoky, 1989; Murphy, Brantley, Blum, White,

& Dong, 1998). During weathering, biotite expands in the direction normal to its sheets, exerting stress on the surrounding matrix (Bisdom, Stoops, Delvigne, Curmi, & Altemuller, 1982; Takaya, Hatta, & Matsukura, 2014).

Biotite expansion can occur by multiple mechanisms. First, interlayer potassium cations can be replaced by hydrated magnesium cations, which thickens a single biotite layer from 10 Å to 14 Å, and induces minimal changes in the layer's lateral dimensions (e.g., Bisdom et al., 1982). Second, Fe^{2+} cations can be oxidized into Fe^{3+}, producing altered biotite with an expansion of the (001) d-spacing from 10 Å to 10.5 Å (Dong et al., 1998). The first of these mechanisms involves the greatest volume expansion and therefore has the greatest potential to damage rock. In this study we thus restrict our attention to this mechanism, following previous studies (Buss et al., 2008; Goodfellow et al., 2016).

The REV consists of two phases: biotite and matrix. The matrix is a single homogeneous phase, while the biotite phase may contain an infinite number of inclusion orientations and aspect ratios. For simplicity in our simulations, we apply the same aspect ratio and orientation to groups of biotite inclusions, as this facilitates exploration of biotite characteristics on bedrock weakening.

The assumed oblate spheroidal shape of the inclusions in Section 2.1 differs from the geometry of biotite crystals in nature, which are closer in shape to rectangular prisms than oblate spheroids. This geometric approximation allows us to capture several essential characteristics of biotite weathering and bedrock damage. First, it captures the fact that biotites tend to be relatively flat, thinner in one dimension than in the other two. Second, it allows us to represent biotite expansion as a change of mineral aspect ratio without changing the mineral's length along its long axis. We assume that the long axis a remains constant during weathering, such that the chemically-driven strain in the a-direction (ϵ_a^c) is 0. Biotite chemical weathering drives expansion only in the c direction.

To capture the expansion of biotite during chemical weathering, we begin with a parameterization for the production rate of weathered biotite, dQ/dt, within the REV:

$$\frac{dQ}{dt} = RS \tag{12}$$

Here Q (mol) is the number of moles of weathered biotite in the REV, R (mol m^{-2} s^{-1}) is the chemical weathering rate of biotite per unit mineral surface area, and S (m^2) is the total biotite surface area within the REV. Since weathered biotite is produced at the expense of unweathered biotite, Q is equivalent to the number of moles of biotite that are lost during biotite chemical weathering. Note that the form of Equation 12 for biotite may differ from that for other mineral phases, in which the weathered secondary mineral phase may not be produced at the same rate that the primary mineral phase is lost.

We use the weathered biotite production rate to calculate the rate of change of the volume of weathered biotite V_b^w (m^3) in the bedrock REV, to which we assign a value of zero at the onset of biotite chemical weathering.

$$\frac{dV_b^w}{dt} = v_m \frac{dQ}{dt} \tag{13}$$

Here v_m is the molar volume of weathered biotite: $v_m = 2.10 \times 10^{-4}$ m^3 mol^{-1}. Changes in V_b^w are calculated by integrating Equation 13 over time.

The time-varying value of V_b^w is useful because it permits calculation of the evolution of the chemically-driven strain fields in the biotite inclusions (Section 2.1), which in turn permits the calculation of the evolution of the bedrock REV's mechanical properties (Section 2.3). Since the transformation of biotite into weathered biotite involves

minimal changes in the biotite layers' lateral dimensions, the change of volume of the biotite crystals translates into a unidirectional deformation. The change in V_w in Equation 13 is the chemically-induced change in volume that would occur in the absence of the surrounding matrix. Because the matrix inhibits biotite expansion, the total change in biotite volume is smaller than it would be in the absence of matrix. The mechanical interactions between the matrix and chemically-induced biotite expansion is a core aspect of the modeled evolution of damage, as described in Section 2.2.

For this application to biotite weathering, we adopt a parameterization for R as a decreasing power-law function of time, following empirical observations of biotite chemical weathering (White & Brantley, 2003):

$$R = 3.001 \times 10^{-5}\, t^{-0.603} \tag{14}$$

in which the time (t) is the time since the onset of weathering, expressed in years. This equation is a highly simplified parameterization for biotite weathering that nonetheless captures one of its key characteristics: the decline in reactivity over time. It is applied here with the intent of illustrating the model behavior as simply as possible. It is beyond the scope of this study to investigate the model's sensitivity to environmental parameters, but we note that this part of the model could to be modified to do so. Different parameterizations for biotite weathering can be applied here to investigate the model's sensitivity to a variety of factors, including porewater solute concentrations (Maher, 2010), dissolved oxygen concentrations (Fletcher et al., 2006), pH (Bray et al., 2015) and temperature (Ferrier, Kirchner, & Finkel, 2012).

The volume of a biotite inclusion increases during chemical weathering from its initial volume $V_{b,initial}$ to the sum of V_b^w and the remaining unweathered biotite volume, V_b. Since the transformation of a layer of biotite into a layer of weathered biotite increases the layer's thickness by a factor of 1.4, the remaining unweathered biotite volume can be written as $V_b = V_{b,initial} - V_b^w/1.4$. Use of this expression for V_b permits the chemical strain in the thickness direction, ϵ_c^c, to be calculated as follows.

$$\epsilon_c^c = \frac{V_b^w + V_b}{V_{b,initial}} - 1 = \frac{V_b^w(1 - \frac{1}{1.4})}{V_{b,initial}} \tag{15}$$

In the case of complete biotite weathering, for example, V_b^w would be $1.4V_{b,initial}$, and ϵ_c^c would be 0.4. This is the upper limit on ϵ_c^c.

3 Results: Simulation of bedrock damage by biotite weathering

To explore the effects of biotite characteristics (abundance, orientation, and aspect ratio) and boundary conditions on bedrock damage, we conducted a range of simulations with the model presented in Section 2. To do this, we simulated bedrock chemical weathering at the material point, which is at the centroid of the REV and defines our scale of observation. The bulk and shear moduli of biotite, vermiculite and matrix material listed in Table 1 (Abidi, Joliff, & Favotto, 2016; Moos, Dvorkin, & Hooks, 1997). To simulate a rock similar to granite, we assume that the mechanical properties of the bedrock matrix are similar to those of quartz and feldspar, and are similar to the mechanical properties of granite reported by Halm and Dragon. The damage propagation threshold of the matrix is given by the term $k_0 + k_1\Omega$ in Equation 2. The values of damage initiation threshold k_o and damage hardening parameter k_1 were taken equal to the granite parameters found by Halm and Dragon (2002).

We are unaware of measurements of the elastic behavior of weathered biotite. Linear elastic moduli of biotite and vermiculite (not weathered biotite) were published in (Moos et al., 1997) and (Abidi et al., 2016). Based on this, we assume that weathered and unweathered biotite crystals are linear elastic materials, and that inelastic effects

are accounted for via the chemical strain of the inclusion. The elastic moduli of unweathered and weathered biotite that we adopt in this model are reported in Table 1.

According to Jin, Xu, Arson, and Busetti (2017), the maximum damage threshold above which the proposed CDM model is no longer valid is 0.2 (above this threshold, the model would have to be improved to account for the presence of micro-cracks that interact). We thus stopped the simulations whenever damage grew as high as 0.2.

Table 1. Mechanical parameters in bedrock

Biotite		Vermiculite		Matrix					
K_b	μ_b	K_v	μ_v	K_m	μ_m	k_0	k_1	α	β
76700	41600	13824	5300	60700	31300	0.11	2.2	−16000	−31000

K_* and μ_* are respectively the bulk modulus and shear modulus. All parameters are in MPa. (Abidi et al., 2016; Halm & Dragon, 2002; Moos et al., 1997)

3.1 Influence of boundary conditions

During biotite chemical weathering, the evolution of rock damage is influenced by the boundary conditions imposed on the REV because they influence the evolution of stress and strain within the biotites and the matrix. To assess the influence of the boundary conditions on bedrock weakening, we ran a series of simulations with identical biotite characteristics and a range of boundary conditions. In these simulations, biotite abundance is 15% (typical in granite), all biotite inclusions have the same initial aspect ratio $a/c = 3$, and all biotite inclusions are aligned with their long axis (a) oriented at $\theta = 30°$ from the horizontal. The REV thus contains only two components in these simulations: the matrix and one biotite inclusion set.

For the vertical boundary condition, we consider a bedrock REV at depth h subjected to a vertical stress $\sigma_v = \rho g h$, where ρ is the average density of the overlying material (saprolite and soil) and g is gravitational acceleration (9.8 m s^{-1}). For the horizontal boundary condition, we consider the proportional stress boundary condition and the oedometric boundary condition (Figure 2). In the proportional stress boundary condition, the REV is constrained horizontally by a lateral boundary stress $\sigma_h = K\sigma_v$. Here the lateral boundary stress is proportional to the overburden, and K is the ratio between the horizontal and vertical stresses. In the oedometric condition, the REV is constrained to have zero horizontal displacement at the lateral boundaries. This mimics the boundary conditions in so-called oedometer deformation tests in the laboratory, which in nature would be analogous to exceptionally rigid lateral boundaries. While strict oedometric boundary conditions may be less common in nature than proportional stress boundary conditions, we apply both of these boundary conditions in the following simulations because they represent two end-member scenarios that illustrate the range of model behaviors. It is expected that biotite weathering will have the lowest (respectively highest) influence on matrix damage under the proportional stress (respectively oedometric) boundary conditions.

Figure 3 shows the results of six simulations that illustrate the sensitivity of bedrock evolution to the boundary conditions. Each simulation shows how strain within biotites (Figures 3(a) and 3(b)) generates strain in the surrounding matrix (Figure 3(c)), which in turn generates damage (Figure 3(d)). Here, ϵ_c and ϵ_a denote the strains within biotite inclusions in the directions of inclusion thickness c and inclusion radius a, respectively (Figure 1). Similarly, ϵ_v denotes the volumetric strain of the bedrock REV.

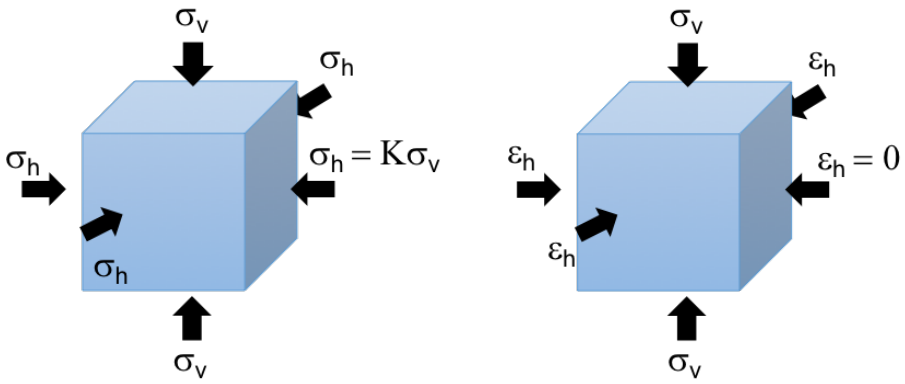

(a) Proportional stress condition (b) Oedometric condition

Figure 2. Schematic of the boundary conditions.

For each of the proportional stress and oedometric boundary conditions, we conducted four simulations at overburden stresses of σ_v = 19.6, 196, 1,960, and 19,600 kPa. For an overburden density of 2000 kg m^{-3} (Grant, 1962), these correspond to depths of ∼1, 10, 100, and 1000 m. In the simulations with the proportional stress conditions, we assign a value of $K = 0.5$ for the stress coefficient (da Fonseca & e Sousa, 2001). In simulations with the oedometric conditions, lateral boundary stresses are not imposed because they evolve under the constraint of no lateral displacement at the boundary.

The simulations are initialized without eigenstrain in the inclusions and without damage in the matrix. We then calculate the weathering rate and the volume of weathered biotite for each inclusion set at each incremental time step. The strain and stress fields of each component of the REV and of the REV overall are then updated. If the matrix damage driving force exceeds the damage threshold, then the damage of the matrix is updated from the consistency conditions.

To further investigate the effects of boundary conditions, we conducted six more simulations under the proportional stress condition and a range of values for the stress coefficient K, which controls the magnitude of the horizontal boundary stresses relative to the vertical boundary stress. In each of these simulations the vertical boundary stress σ_v is set to 196 kPa, roughly equivalent to 10 m of overburden with density 2000 kg m^{-3}, which is comparable to the thickness of many weathering extents in bedrock, e.g., (Buss et al., 2017; West, 2012).

Figure 3 shows that bedrock damage (Ω) initiates hundreds of years earlier under the oedometric boundary condition than under the proportional stress boundary condition, and exhibits minor sensitivity to depth. Figure 4 shows that strain and damage are insensitive to the choice of K. All six simulations, with values of K ranging from -1 (lateral tension) to 10 (strong lateral compression), are indistinguishable from one another in Figure 4. For comparison, Figure 4 also shows one simulation under the oedometric condition (dashed line), in which damage initiates hundreds of years earlier than under the proportional stress boundary condition. We ran a series of simulations with aligned biotite inclusions oriented at $\theta = 0°$, $\theta = 60°$, and $\theta = 90°$, and we observed the same trends as those shown in Figures 3 and 4.

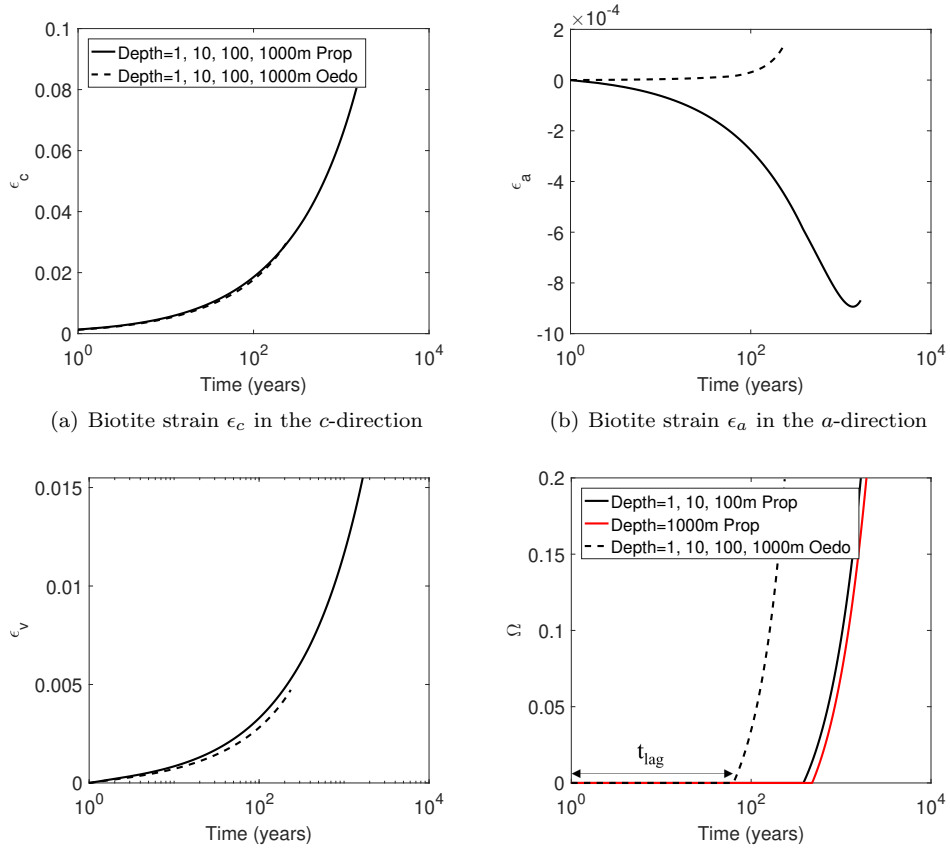

(a) Biotite strain ϵ_c in the c-direction

(b) Biotite strain ϵ_a in the a-direction

(c) Volumetric strain of bedrock REV

(d) Damage in the matrix

Figure 3. Effects of boundary conditions on strain and damage. **a.** Biotite strain in the thickness direction c (ϵ_c) increases over time and shows negligible sensitivity to depth and boundary conditions (proportional stress vs. oedometric boundary conditions). **b.** Biotite strain in the transverse direction (ϵ_a) is ∼100 times smaller than ϵ_c. It exhibits contraction under the proportional stress condition, expansion under the oedometer condition, and negligible sensitivity to depth. **c.** Volumetric strain in the bedrock REV (ϵ_v) is small (<2%) and exhibits negligible sensitivity to depth and only minor sensitivity to boundary conditions. **d.** The time until damage initiation is noted as t_{lag}. Bedrock damage (Ω) initiates hundreds of years earlier under the oedometric condition than under the proportional stress condition, and exhibits minor sensitivity to depth. In each simulation, initial biotite abundance was 15%, initial biotite aspect ratio was 3, and the initial orientation of all biotite a-axes were 30° relative to the horizontal.

3.2 Influence of biotite abundance

To illustrate the effects of biotite abundance on bedrock damage, we show the results of three simulations with biotite abundances of 5, 10, and 15% by volume. In each simulation the vertical boundary stress is 196 kPa, equivalent to a depth of 10 m under material with a density of 2000 kg m^{-3}, typical of saprolite. Since strain and damage are relatively insensitive to lateral stresses at that depth (Figure 4), K is set to 0.5 in all simulations under proportional stress. The initial aspect ratio of biotite inclusions was set to 3 and all biotite inclusions were aligned at $\theta = 30°$, like in the simulations in Section 3.1.

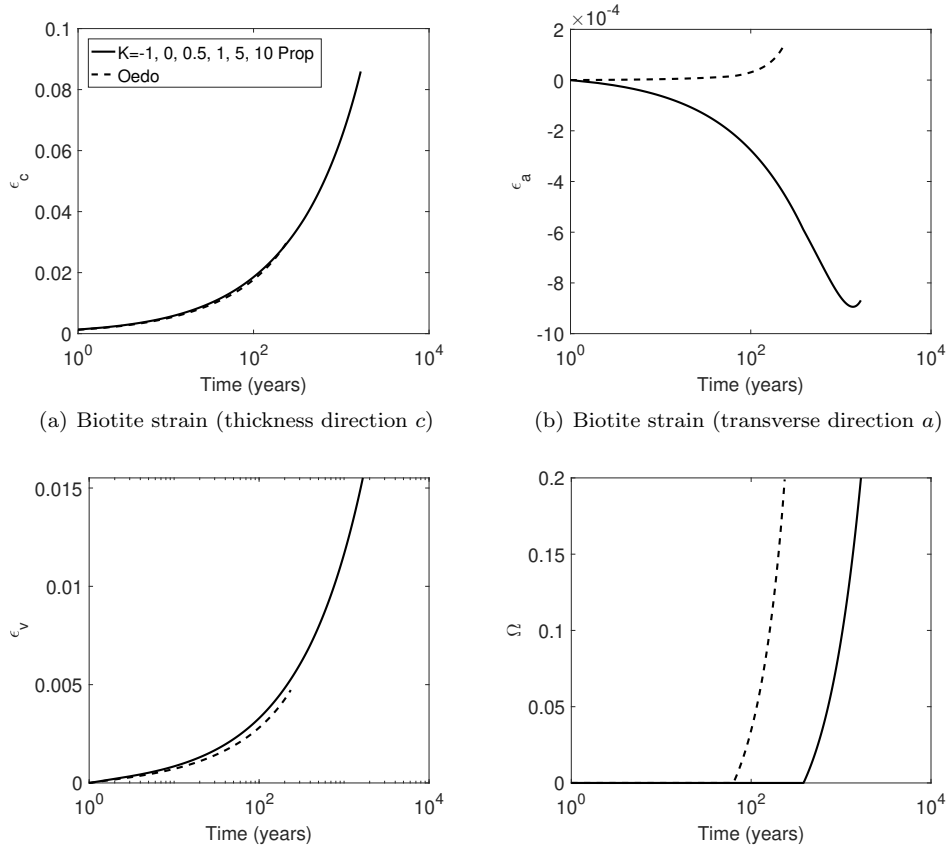

(a) Biotite strain (thickness direction c)

(b) Biotite strain (transverse direction a)

(c) Volumetric strain of bedrock REV

(d) Damage in the matrix

Figure 4. Effect of the stress coefficient (K) on strains and damage under the proportional stress boundary condition. **a.** Biotite strain in the thickness direction (ϵ_c) shows negligible sensitivity to K. **b.** Biotite strain in the transverse direction (ϵ_a) also shows negligible sensitivity to K. **c.** The REV volumetric strain (ϵ_v) is small (<2%) and exhibits negligible sensitivity to K. **d.** Bedrock damage (Ω) exhibits minor sensitivity to K. In each simulation, the initial biotite abundance was 15%, the initial biotite aspect ratio was 3, and the initial orientation of all biotite a-axes were 30° relative to the horizontal.

Fig. 5 shows the influence of biotite abundance on strains and damage under the proportional stress boundary condition. Figure 5(a) reveals that biotite abundance has only negligible effects on biotite expansion in the direction of biotite thickness, with marginally greater biotite expansion at higher biotite abundance. Radial biotite shrinkage is small ($< 0.3\%$) but grows larger at lower biotite abundances (Fig. 5(b)). Figure 5(c) shows that the REV strain ϵ_v increases with biotite abundance, and Figure 5(d) shows that damage initiates earlier in rocks with higher biotite abundances. The damage accumulation rate does not depend on biotite abundance (i.e., the damage evolution curves are parallel to each other in Fig. 5(d)). For comparison, Appendix B.1 presents an additional set of simulations that show that biotite abundance has similar effects on strain and damage under oedometric boundary conditions.

3.3 Influence of biotite aspect ratio

The effect of biotite aspect ratio on strains and damage under proportional stress condition is presented in Fig. 6. In all simulations, the initial biotite abundance is 15%,

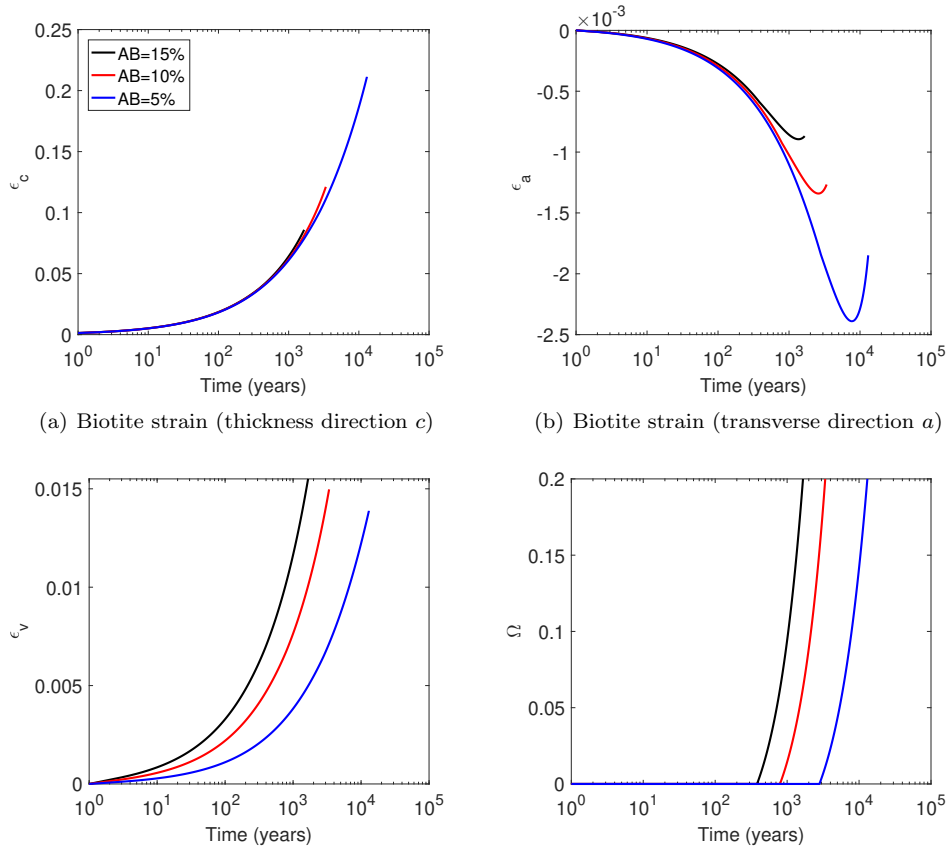

(a) Biotite strain (thickness direction c)

(b) Biotite strain (transverse direction a)

(c) Volumetric strain of bedrock REV

(d) Damage in the matrix

Figure 5. Effect of biotite abundance (AB) on strains and damage under the proportional stress boundary condition. **a.** Biotite strain in the thickness direction (ϵ_c) increases over time and shows negligible sensitivity to abundance until the initiation of damage. **b.** Biotite strain in the transverse direction (ϵ_a) exhibits larger contraction in rocks with lower biotite abundances. **c.** The REV volumetric strain (ϵ_v) increases with biotite abundance. **d.** Bedrock damage (Ω) initiates earlier at higher biotite abundances. In each simulation, the initial biotite aspect ratio was 3, the depth of the bedrock was 10 m, and the initial orientation of all biotite a-axes was 30° relative to the horizontal.

biotite inclusions are initially aligned at $\theta = 30°$, and the vertical boundary stress is 196 kPa. We conduct simulations under four scenarios: three in which all biotites share the same initial aspect ratio (either 3, 6, or 9), and one with three equally abundant biotite inclusion sets, one with an aspect ratio of 3 and the other two with aspect ratios of 6 and 9. In the first three cases, the REV contains only two components (matrix and one biotite inclusion set), while in the fourth case, the REV contains four components (matrix and three biotite inclusion sets).

Figures 6(a) and 6(b) show that the deformation of biotite inclusions is almost entirely insensitive to biotite aspect ratio. Figure 6(c) shows that volumetric expansion of the matrix grows larger under smaller biotite aspect ratios before the threshold damage of 20% is reached, though in all cases the volumetric strain is less than 1%. By contrast, Figure 6(d) shows that the time to the initiation of damage is sensitive to biotite aspect ratio, especially for simulations under the proportional stress boundary condition. Figure 6(d) further shows that the simulation with a uniform distribution of aspect ratios

476 (AR = 3, 6, 9) lies between the simulations with AR = 3 and AR = 6, which suggests
477 that inclusions of lower aspect ratio dominate the development of damage in the matrix.
478 For comparison, the influence of biotite abundance under oedometric condition is pre-
479 sented in Appendix B.2.

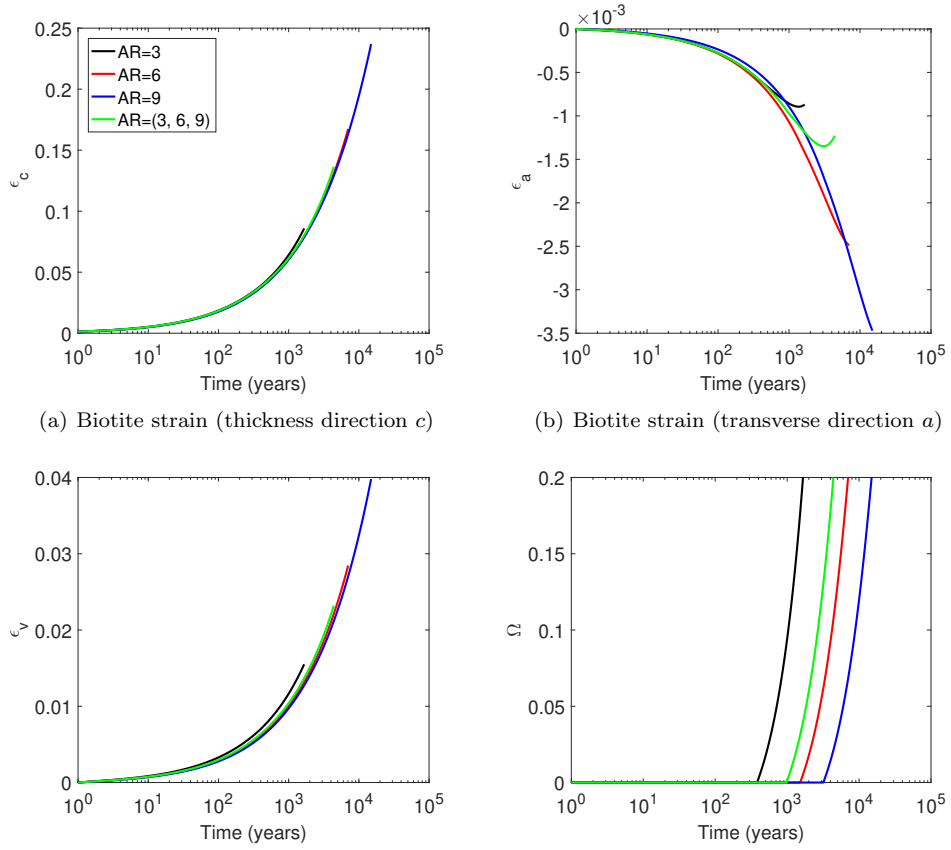

(a) Biotite strain (thickness direction c)

(b) Biotite strain (transverse direction a)

(c) Volumetric strain of bedrock REV

(d) Damage in the matrix

Figure 6. Effect of biotite aspect ratio (AR) on strains and damage. **a.** Biotite strain in the thickness direction (ϵ_c) shows negligible sensitivity to aspect ratio. **b.** Biotite strain in the transverse direction (ϵ_a) exhibits minor sensitivity to aspect ratio. **c.** The REV volumetric strain (ϵ_v) exhibits slightly larger expansion at smaller aspect ratios. **d.** Bedrock damage (Ω) initiates earlier in rocks with biotites with smaller aspect ratios. In each simulation, initial biotite abundance was 15%, the depth of bedrock is 10 m, and the initial orientation of all biotite a-axes were 30° relative to the horizontal.

480 ### 3.4 Influence of biotite orientation

481 The third biotite characteristic we investigated is orientation. To study its effect,
482 we conducted a series of simulations under a range of biotite orientations. In each sim-
483 ulation, the REV contains one set of identical biotite inclusions, which share an initial
484 aspect ratio of 3 and an initial aligned orientation θ (Figure 1(b)) of either 0, 30, 45, 60,
485 90°. We also simulated the case of uniformly distributed orientations (UD). The initial
486 biotite abundance in each simulation is 15%.

In order to simulate the damage accumulation in the bedrock with uniformly distributed biotite, we used 74 distinct orientations distributed on the unit sphere, following Bažant's discrete integration scheme (Bažant & Oh, 1986).

The solid lines in Figure 7 show that orientation of aligned biotite has a negligible effect on the development of strain or damage under the proportional stress boundary condition. In each panel of Figure 7, the lines for simulations at all orientations with aligned biotite overlap with each other within the width of the plotted line. When biotite is uniformly distributed, the effects of biotite weathering on the matrix accumulate in different directions, which retards the initiation of damage.

In Figure 7, the dashed lines refer to the simulations done with aligned inclusions. Results show that strain and damage are sensitive to biotite orientation under the oedometric boundary condition, unlike under the proportional stress condition. Figure 7(d) shows that damage initiates earlier under the oedometric boundary condition than under the proportional stress condition, except for the simulation with $\theta = 0°$, which shares almost the identical evolution as all proportional stress simulations. This further shows that damage initiates faster at higher values of θ under oedometric conditions than under proportional stress boundary conditions. When the biotite inclusions are uniformly distributed, the triggering of damage happens sooner than for aligned biotites only if $\theta = 0^o$.

4 Discussion

The simulations in Section 3 provide some of the first mechanistic treatments of how biotite expansion affects the transient development of bedrock damage. Despite differences in the initial and boundary conditions between simulations, there are several common behaviors that emerge in all simulations: 1) Biotites thicken monotonically by a large amount (9-20% in $\sim 10^3$ to 10^4 years); 2) Biotites grow or shrink in the transverse direction by a small amount ($< 0.3\%$); 3) The bedrock REV volumetric strain increases monotonically but always remains small ($< 2\%$); 4) After the onset of biotite chemical weathering, no damage occurs for decades to millennia; 5) After damage initiates, it grows rapidly to the upper threshold of 20%, where the continuum approximation breaks down and simulations are terminated. These behaviors are modulated by the boundary conditions imposed on the rock (Figures 3-4), as well as by biotite abundance (Figure 5), aspect ratio (Figure 6), and orientation (Figure 7).

The time lag between the onset of biotite chemical weathering and the onset of damage, t_{lag} (Figure 3(d)), is one of the key characteristics of the model behavior. Damage occurs when the damage criterion f_d exceeds 0 with the increase of strain in the matrix (Equation 2), while the damage driving force controlled by the matrix strain remains below the damage threshold at earlier times during the chemical weathering process. This time lag t_{lag} is of interest because it indicates when damage starts developing in the matrix, and is a consequence of the damage threshold term k_0. It is also the characteristic that is most sensitive to biotite chemical weathering in our simulations, exhibiting a range of roughly two orders of magnitude under a range of biotite characteristics. Figure 8 shows that damage initiates earlier at higher biotite abundances (Figure 8(a)), smaller aspect ratios (Figure 8(b)), and, under oedometric boundary conditions, for biotites whose a-axes are oriented at a larger angle compared to the horizontal (Figure 8(c)). Here we discuss how the development of damage and strain are affected by the boundary conditions and biotite characteristics, including abundance, aspect ratio, and orientation.

4.1 Sensitivity to boundary conditions

Our simulations illustrate the sensitivity of damage development to both vertical and horizontal boundary conditions. Figure 3(d), for example, shows that damage ac-

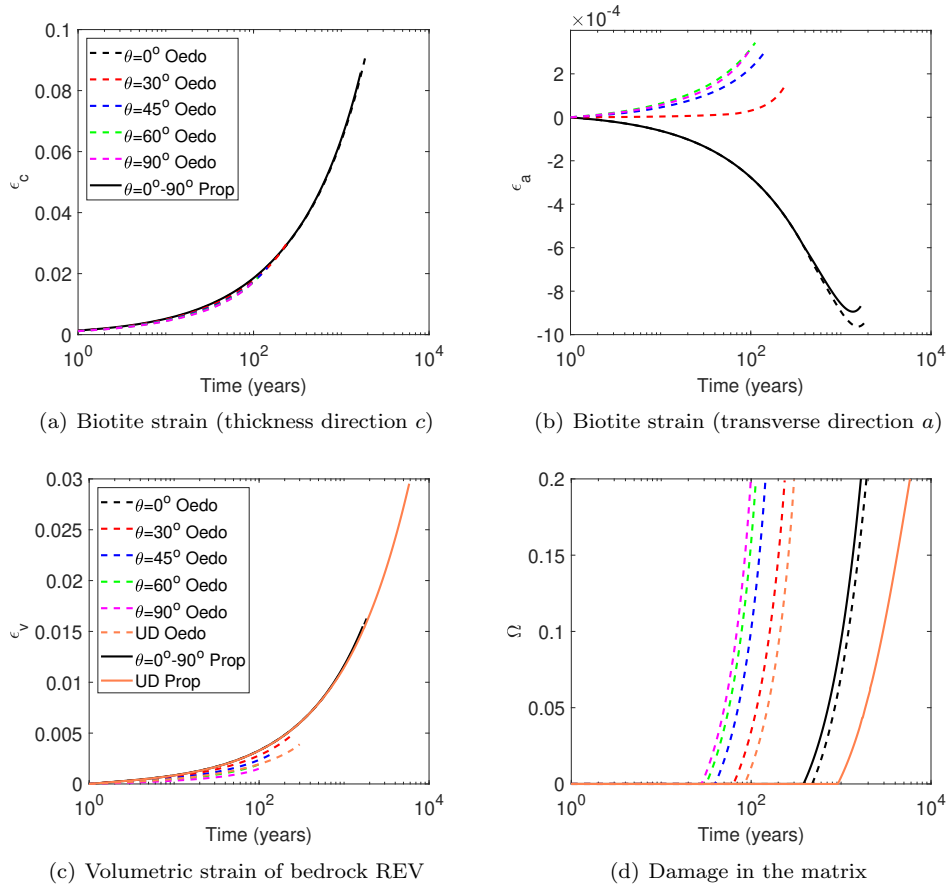

(a) Biotite strain (thickness direction c)

(b) Biotite strain (transverse direction a)

(c) Volumetric strain of bedrock REV

(d) Damage in the matrix

Figure 7. Effect of biotite orientation (θ) on strains and damage. **a.** Biotite strain in the thickness direction (ϵ_c) exhibits minor sensitivity to orientation. **b.** Biotite strain in the transverse direction (ϵ_a) shows negligible sensitivity to orientation under proportional stress boundary conditions, and exhibits larger expansion in rocks with larger θ under oedometric boundary conditions. **c.** The REV volumetric strain (ϵ_v) exhibits minor sensitivity to orientation under the proportional stress boundary condition, and decreases with θ under the oedometric boundary condition. **d.** Bedrock damage (Ω) initiates earlier in rocks with larger θ under the oedometric boundary condition. In each simulation, initial biotite abundance is 15%, the initial biotite aspect ratio is 3, and the depth of the REV is 10 m under overburden with a density $\rho = 2000$ kg m^{-3}.

cumulates later in deeper rocks. This is because deeper rocks have larger vertical overburden pressures that more strongly counteract the inclusion strains and matrix stresses that build up due to biotite expansion. At greater depths, damage initiates later because it takes longer for biotite-driven stresses to overcome the overburden stress that inhibits damage. This illustrates the importance of the upper boundary condition that determines the vertical stress on the REV.

The same simulations in Figures 3 and 4 illustrate the importance of the lateral boundary conditions. For example, in the oedometric boundary conditions simulations in Figure 3(c), damage initiates after a relatively short time (< 100 years) even though the volumetric strain is still low ($< 0.3\%$). By contrast, in the simulations under proportional stress boundary conditions, damage initiates later (after several hundreds of years) at a time when volumetric strain has grown several times larger ($0.5-0.6\%$). This dependence on the lateral boundary condition occurs because the strain in the matrix

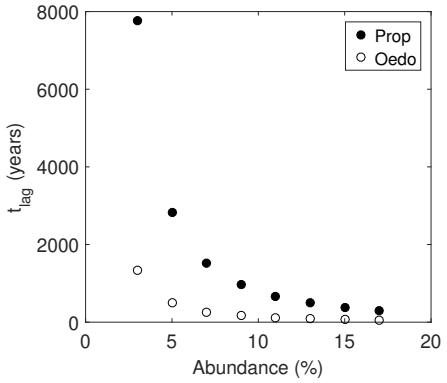

(a) Biotite abundance with biotite aspect ratio = 3 and $\theta = 30°$

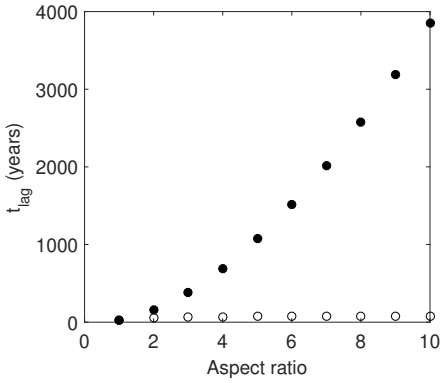

(b) Biotite aspect ratio (a/c) with biotite abundance = 15% and $\theta = 30°$

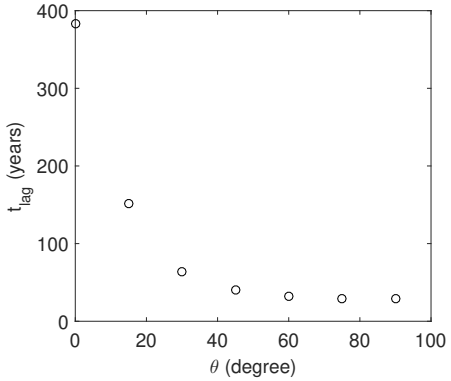

(c) Biotite orientation with biotite abundance = 15% and biotite aspect ratio = 3

Figure 8. The effects of boundary conditions and biotite characteristics on damage initiation: simulation results obtained with proportional stress boundary conditions (filled circles), and with oedometric boundary conditions (open circles). In each simulation, the depth of the REV is 10 m. For the proportional boundary condition, $K = 0.5$.

increases rapidly with the expansion of biotite if the total lateral displacement is fixed. Unless all biotite inclusions are oriented horizontally, the expansion of the biotite inclusions induces a lateral stress in the bedrock REV. Imposing a condition of no lateral displacement on the lateral boundaries of the REV thus induces a compressional strain in the matrix, which results into a tensile difference of principal strains and accelerates the initiation of damage. Under the proportional stress boundary condition, by contrast, the matrix strain build-up is relatively slower, because the REV can expand despite the imposed lateral confinement stress.

One of the most striking results is that the lateral confining stresses under the proportional stress boundary conditions do not have any influence on damage accumulation rates (Figure 4). Here, applying a K value as great as 10—where lateral compressive stresses are 10 times the overburden stress—produces only minute differences in damage development relative to that in simulations with $K < 1$ (lateral tension). This suggests that bedrock damage during biotite oxidation is divorced from regional or topographic stresses, which are often implicated in fracturing near surface bedrock (e.g., Miller & Dunne, 1996; Moon, Perron, Martel, Holbrook, & St. Clair, 2017; Slim, Perron, Martel, & Singha, 2015; St. Clair et al., 2015).

4.2 Sensitivity to biotite abundance

The biotite characteristic that exerts the strongest control on damage development is abundance. Indeed, biotite abundance has almost as much influence on damage accumulation as the difference between the proportional stress and oedometric boundary conditions. Figure 8(a) shows that biotite abundance has a nonlinear influence on damage development. Increasing biotite abundance by a factor of three from 5% to 15%, for example, decreases the time to the onset of chemical damage by roughly a factor of ten. However, as biotite abundance increases, further increases in biotite abundance induce progressively smaller decreases in t_{lag}.

As described in Section 2, the initiation and evolution of damage is determined by the strain of the matrix, which depends on the double dot product of the concentration tensor and the REV strain (Equation 10). Because both the concentration tensor and the REV strain tensor are nonlinear functions of biotite abundance (Equations 7 and 9), biotite abundance has a nonlinear effect on damage development. Physically, this nonlinear behavior comes from the non-linear relationship between the chemical weathering rate and the weathered volume of biotite, as well as from the non-linear interaction between the deformation field of the inclusions and that of the matrix.

4.3 Sensitivity to biotite aspect ratio

Like abundance, aspect ratio exerts a significant influence on damage development. Our simulations show that biotites with smaller aspect ratios damage rock faster than biotites with larger aspect ratios (Figure 8(b)). This effect is most apparent for the proportional stress boundary condition, in which lateral horizontal stresses are proportional to overburden stresses. Oedometric boundary conditions, by contrast, appear to dampen the influence of biotite aspect ratio (Figure 8(b)).

For a biotite inclusion of a given volume and fixed radius a, the c dimension (thickness) decreases when the biotite aspect ratio a/c increases. It follows that, for a given volume fraction of biotite inclusions in the REV, the number of expandable layers in the biotite inclusions decreases when the aspect ratio increases. As a result, the strain rate of the biotite inclusions also decreases when the aspect ratio increases, such that matrix strains take longer to accumulate under the chemical weathering of biotites with larger aspect ratios. The consequence is that the time lag to the onset of damage increases with aspect ratio.

Figure 6 shows that bedrock damage is nonlinearly related to biotite aspect ratio. In this figure, one of the simulations was conducted on bedrock with a mixture of three equally abundant biotite inclusion sets with aspect ratios of 3, 6, and 9. If damage were linearly related to aspect ratio, then the resulting damage would match that in the simulation for biotites with the mean aspect ratio (6), but here it does not. Instead, its damage evolution curve lies between the evolution curves for biotites with aspect ratios of 3 and 6. This implies that damage propagation is dominantly controlled by biotites with small aspect ratios under the proportional stress boundary condition.

4.4 Sensitivity to biotite orientation

Figure 7 shows that biotite orientation θ influences damage accumulation under certain boundary conditions but not others. Under the proportional stress boundary condition, strain and damage evolve identically under all orientations. By contrast, under the oedometric boundary condition, θ does affect the evolution of strains and damage.

We can gain an understanding for why this occurs by considering the end member orientations $\theta = 0^\circ$ and $\theta = 90^\circ$. First consider the scenario $\theta = 0^\circ$. Here, biotites are aligned horizontally and expand in the vertical direction. Because chemically-

driven biotite expansion is perpendicular to the lateral boundaries, it is unaffected by the lateral boundary condition. As a result, biotite expansion produces identical matrix stresses—and hence identical biotite and matrix strains and damage—under the proportional stress and oedometric boundary conditions.

Now consider the opposite end member scenario of $\theta = 90°$. Here, biotites expand in the horizontal direction. Under proportional stress boundary conditions, the matrix can expand in the the lateral direction, like in the case $\theta = 0°$. The mechanical response of the matrix is thus similar for $\theta = 0°$ and $\theta = 90°$. By contrast, under the oedometric boundary condition, the matrix cannot expand laterally because it is constrained by the fixed horizontal position of the boundary. As a result, compressive strains accumulate in the matrix, which accelerates the initiation of damage.

We can generalize from these end member scenarios to the general dependence of strain and damage on biotite orientation. Under the proportional stress boundary condition, biotite orientation has no effect on strain or damage because rotating the biotite inclusions is equivalent to rotating the tectonic stresses. Stress in the matrix is controlled by inclusions' eigenstrains, and not by the tectonic stresses. Therefore, the orientation of the biotite inclusions has negligible influence on the development of damage in the matrix.

Under the oedometric boundary condition, by contrast, as θ increases, the expansion of biotite leads to progressively larger lateral compressive stress in the matrix because the boundaries inhibit lateral strain. As shown in Fig. 7(d), this leads to an earlier initiation of damage. Similarly, because increasing θ leads to progressively less confinement in biotite's transverse direction, ϵ_a tends to increase with θ, as shown in Fig. 7(b). Thus, for all biotite orientations other than $\theta = 0°$, the fixed lateral boundaries under oedometric boundary conditions limit biotite expansion in its thickness direction but promote expansion in its transverse direction. The net result is that deviatoric stresses in the matrix grow faster at higher values of θ, which produces earlier initiation of damage.

As shown in Figure 7, under the proportional stress boundary condition, damage initiates later when biotite orientations are uniformly distributed than when biotite inclusions are aligned, because stress redistribution in the matrix is roughly equal in all directions of space. This confirms that damage due to weathering is insensitive to the lateral stress. Under oedometric boundary conditions, the redistribution of stress in the matrix is affected by the constraint on horizontal displacements, which accelerates the onset of damage, except when biotites are oriented at an angle of $\theta = 0^o$, i.e. parallel to the horizontal, in which case, biotite vertical expansion is not strongly hindered. With a uniform distribution of biotite orientations, damage occurs later than with non-horizontal aligned inclusions, because biotite expansion in multiple directions of space generates counteracting stresses in the matrix – because of the same mechanisms as under proportional loading. Results confirm that a bedrock with horizontal biotite inclusions yields a very special case under oedometric conditions - the only case when damage triggering occurs at the same time as under proportional loading.

4.5 Controls on biotite and matrix strains

Figure 3(b) shows that the depth of the REV does not influence the lateral strain of the inclusions (ϵ_a). Instead, ϵ_a increases with the propagation of damage. Under proportional stress boundary conditions, the radius of biotite inclusions decreases during biotite expansion due to the inclusion's Poisson's ratio. Under oedometric boundary conditions, ϵ_a is almost constant, due to the imposed lateral displacements at the REV boundary. Slightly less volume expansion is observed under the oedometric boundary condition in Fig. 3(c).

Figures 3-7 show that biotite strain in the thickness direction (ϵ_c) and its rate of change both increase over time. The similarity in the evolution of ϵ_c in all simulations shows that ϵ_c is nearly independent of depth, lateral boundary conditions, or biotite abundance, aspect ratio, and orientation. This implies that ϵ_c is almost entirely controlled by chemically-driven mineral expansion, and that it is almost entirely insensitive to stress in the surrounding matrix. Both chemical weathering expansion and interaction between matrix and inclusions contribute to the development of ϵ_c. Due to the nonlinear influence of the matrix on the biotite inclusions (Equation 10), ϵ_c grows non-linearly over time.

4.6 Model limitations

The proposed model can successfully be used to predict the initiation of damage in the bedrock and calculate the resulting damaged bedrock mechanical properties as a result of the chemical strain of weathering minerals. While powerful, we stress that this model's applicability is limited by the assumptions underlying it and the scale at which it is relevant. For example: (i) The Mori-Tanaka homogenization scheme accounts for the volume fraction of the inclusions, but cannot distinguish the offsetting effects of inclusion size from those of inclusion number. Thus, within the REV, it cannot distinguish between many small biotites or a few large biotites, provided they have the same total volume, the same aspect ratio and the same orientation. (ii) Our application of the model is restricted to isotropic inclusions, an isotropic matrix, isotropic damage, and either aligned or randomly oriented biotite crystals. The predicted REV stiffness tensor does not always meet the positivity and symmetry requirements when one of the REV components is anisotropic or when the inclusions are either non-uniformly oriented or non-aligned (Pichler & Hellmich, 2010). More work is needed to assess the conditions under which it is reasonable to use the proposed model with non-aligned/non-uniformly aligned inclusions or with anisotropic damage in the matrix. (iii) This is a model for microscopic bedrock damage –not a model of macroscopic fracturing. Thus it cannot compute the development of the macroscale fracture network. Our restriction of the model in this study to small spatial scales is intentional, because upscaling these processes to model macroscopic fracturing (which we are currently developing in a companion study) must build on a microscopic damage model such as this one.

Because our model results are confined to microscopic damage, which is defined strictly in our model as a decrease in stiffness, direct comparisons to typically measured parameters in field and laboratory studies of bedrock weathering are also limited. Recent studies have compared measurements in maximum compressive and tensile strengths to fracture densities and chemical mass losses in weathering rock (Goodfellow et al., 2016; Griffiths, Heap, Baud, & Schmittbuhl, 2017). While these studies reveal correlations between mechanical strength, fracture density, and chemical properties, they are not directly comparable to our model results. However, some qualitative correlations can be made between our model results and these published observations. Tensile and compressive strength tests are commonly used to measure material stiffness, and in granitoid rock, these properties have been shown to correlate with modeled fracture energy density and progression of Fe-oxidation in weathering biotite (Goodfellow et al., 2016). Observations described in these studies suggest that progressive oxidation of Fe in biotite contributes to mechanical weakening via microcrack propagation; through which meteoric fluids can further chemo-mechanically weather bedrock once pore space is connected (Buss et al., 2008; Eppes & Keanini, 2017; Goodfellow et al., 2016). Observational studies suggest that microcrack propagation initiates once available Fe in biotite is 20%-65% oxidized, which may relate to the lag times predicted in our models between spin up and damage development (Goodfellow et al., 2016). Our model results suggest that biotite aspect ratio and abundance are key drivers to mechanical weakening of granitoid rock during biotite oxidation; however these observations are generally absent from the literature. Our model thus serves to elucidate the role of these mineral grain characteristics in the weakening of weathering rock for future studies.

We note that our model is driven by a simplified representation of biotite weathering. In nature, several factors can affect the rate of mineral weathering and coevolve along with it. For example, mineral weathering affects the rock's permeability and connected porosity, which in turn affects fluid transport in the rock and pore water solute concentrations, which affect mineral dissolution rates (Hellmann & Tisserand, 2006; Maher, Steefel, White, & Stonestrom, 2009; White et al., 2008). Chemical weathering triggers the initiation and propagation of cracks, which enhances the porosity of rock, as shown in this study and in (Goodfellow et al., 2016). Higher rock permeability facilitates solute transport and increases oxygen availability for weathering. Conversely, secondary mineral precipitation within pore spaces can reduce the conductivity of rock and may create preferential flow paths (Perillo, Gupta, Nater, & Moncrief, 1999). Secondary mineral precipitation and solute transport moderate primary mineral chemical weathering rates by regulating the mineral saturation state (Maher, DePaolo, & Christensen, 2006) and reducing the reactive surface area (Köhler, Dufaud, & Oelkers, 2003). Redox conditions and concentrations of solutes in the vadose zone play a crucial role in the chemical weathering process (Rempe & Dietrich, 2014; Steefel & Maher, 2009). Future studies could explore the couplings between the bedrock weakening modeled in our study and other hydrologic, climatic, and geochemical characteristics by developing a coupled chemo-hydro-mechanical model. Such a model would need to update solute concentrations, hydraulic properties, and oxygen states in during the chemical weathering process.

5 Conclusions

The primary contribution of this study is the development of a new model for the effects of multi-mineral chemical weathering on the evolution of bedrock damage. Our simulation results on biotite chemical weathering suggest that the physical characteristics of biotite crystals—most importantly aspect ratio and abundance—have a profound effect on the evolution of bedrock damage during biotite chemical weathering. This implies that relatively minor differences in biotite populations between two otherwise similar rock types can drive significant differences in the progression of rock weakening at the microscale. Similarly, this implies that local differences in biotite character could drive differences in damage development within a single pluton. This has compelling implications for a number of weathering processes, including the development of tors, wherein some rock volumes experience minimal weathering and are exposed as bare rock at the Earth's surface, while other rock volumes break down into saprolite and soil (e.g., at the Boulder Creek Critical Zone Observatory in Colorado and the Wind River Range in Wyoming; R. S. Anderson, 2002; Heimsath, Chappell, Dietrich, Nishiizumi, & Finkel, 2001). More broadly, this supports the hypothesis that spatial variations in biotite characteristics can influence the evolution of topography, hydrology, and nutrient supply, consistent with previous studies.

The importance of biotite in bedrock damage motivates future studies of biotite characteristics in bedrock and saprolite at the mineral and field scale. There are many opportunities for progress here. Bedrock biotite abundances are measured relatively infrequently (e.g., Ferrier, Kirchner, Riebe, & Finkel, 2010; Murphy et al., 1998), and biotite aspect ratios are not commonly reported in the literature, so the effect of biotite shape on damage generation remains poorly documented. Future field observations of biotite abundance, aspect ratio, and orientation will be needed to test our model results. Our results further motivate upscaling the model from the microscale evolution of bedrock damage to the macroscale evolution of the fracture network, which will permit investigation of biotite's effects at the saprolite scale.

A Appendix: Resolution algorithm for the homogenization scheme

We use the Mori-Tanaka homogenization scheme to upscale the microscopic stresses and strains in the mineral inclusions and in the matrix to the REV scale. At each time step, the matrix stiffness $\mathbf{C}_o^t$ and the thickness c^t and radius a^t of the mineral inclusions are considered as input variables because they are calculated at the previous time step. The total volume of mineral before the weathering from t to $t+\delta t$ occurs ($V_{mineral}^t$) is obtained from c^t and a^t. In the proposed algorithm (illustrated in Figure A.1), the volume of weathered mineral ${V_{mineral}^w}^t$ is first calculated by substituting Eq. 12 and 14 into Eq. 13. Then, the chemical strains $\epsilon_{cc,i}^t$ (eigenstrains) are updated by using Eq. 15, while the stiffness of mineral inclusions $\mathbf{C}_i^t$ is calculated by using a volume average approximation. At the REV scale, the strain concentration tensor $\mathbf{A}_i^t$ and the influence tensor $\mathbf{D}_{ij}^t$ are calculated, based on the shape and stiffness of the inclusions (c^t, a^t and $\mathbf{C}_i^t$). Using $\mathbf{A}_i^t$ and $\mathbf{D}_{ij}^t$, the homogenized stiffness $\mathbf{C}_{hom}^t$ is updated by means of Eq. 6. Next, the unknown components of the macroscopic stress $\bar{\sigma}$ and of the macroscopic strain $\bar{\epsilon}$ are calculated with Eq. 9, with the given boundary stress and strain conditions. The stresses σ_i^t and the strains ϵ_i^t in each phase are then calculated by using Eq. 5 and Eq. 10. The matrix damage Ω^{t+1} is updated from the strain of the matrix phase. Ω^{t+1} is then used to update the stiffness of the matrix $\mathbf{C}_o^{t+1}$ for the next time step. Then, inclusion shape parameters c^{t+1} and a^{t+1} are calculated from the strain of each inclusion ϵ_i^t, and their values are stored for the next time step.

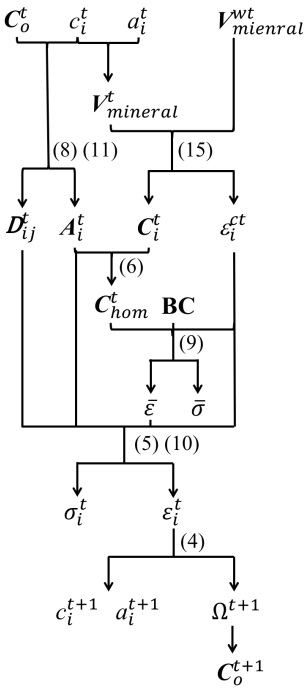

Figure A.1. Resolution algorithm for the proposed homogenization scheme. See the text of Appendix A for the definitions of the variables in this figure.

B Appendix: Effects of abundance and aspect ratio under proportional stress and oedometer conditions

Figure B.1 shows that the effects of abundance on ϵ_c, ϵ_a, ϵ_v, and Ω are similar under proportional stress and oedometric boundary condition. Relative to the proportional

stress boundary conditions, the oedometric boundary conditions induce less contraction of ϵ_a, smaller expansion of ϵ_v, and faster evolution of Ω. Similarly, ϵ_c, ϵ_a, ϵ_v, and Ω all exhibit only minor sensitivity to aspect ratio under oedometric boundary conditions (Figure B.2). This also shows that damage initiates slightly earlier in rocks with biotite inclusions of smaller aspect ratio under oedometric boundary conditions.

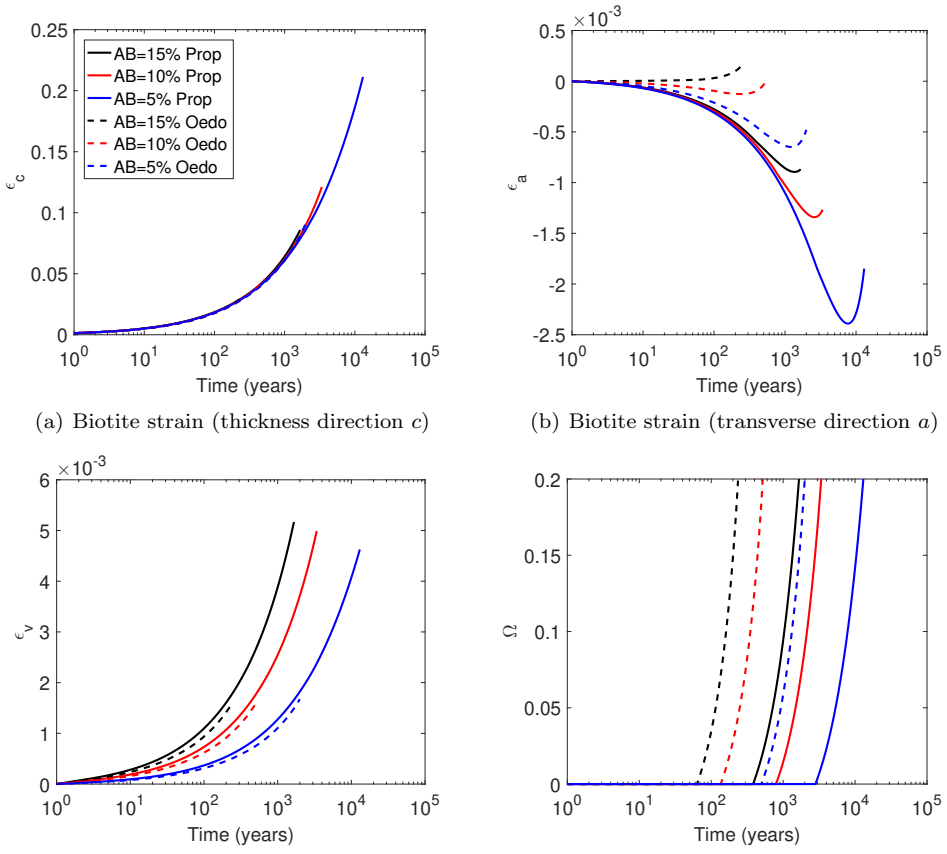

(a) Biotite strain (thickness direction c)

(b) Biotite strain (transverse direction a)

(c) Volumetric strain of bedrock REV

(d) Damage in the matrix

Figure B.1. Effect of biotite abundance (AB) on strains and damage under the proportional stress boundary condition ("Prop") and the oedometric boundary condition ("Oedo"). **a.** Biotite strain in the thickness direction c (ϵ_c) increases over time and shows negligible sensitivity to abundance for both proportional stress and oedometric boundary conditions. **b.** Biotite strain in the transverse direction (ϵ_a) exhibits less contraction under oedometric boundary conditions. **c.** The REV volumetric strain (ϵ_v) increases slower under oedometric boundary conditions. **d.** Bedrock damage (Ω) initiates earlier under oedometric boundary conditions. In each simulation, initial biotite aspect ratio was 3, the depth of bedrock was 10 m, the overburden density was $\rho = 2000$ kg m^{-3}, and the initial orientation of all biotite a-axes were 30° relative to the horizontal.

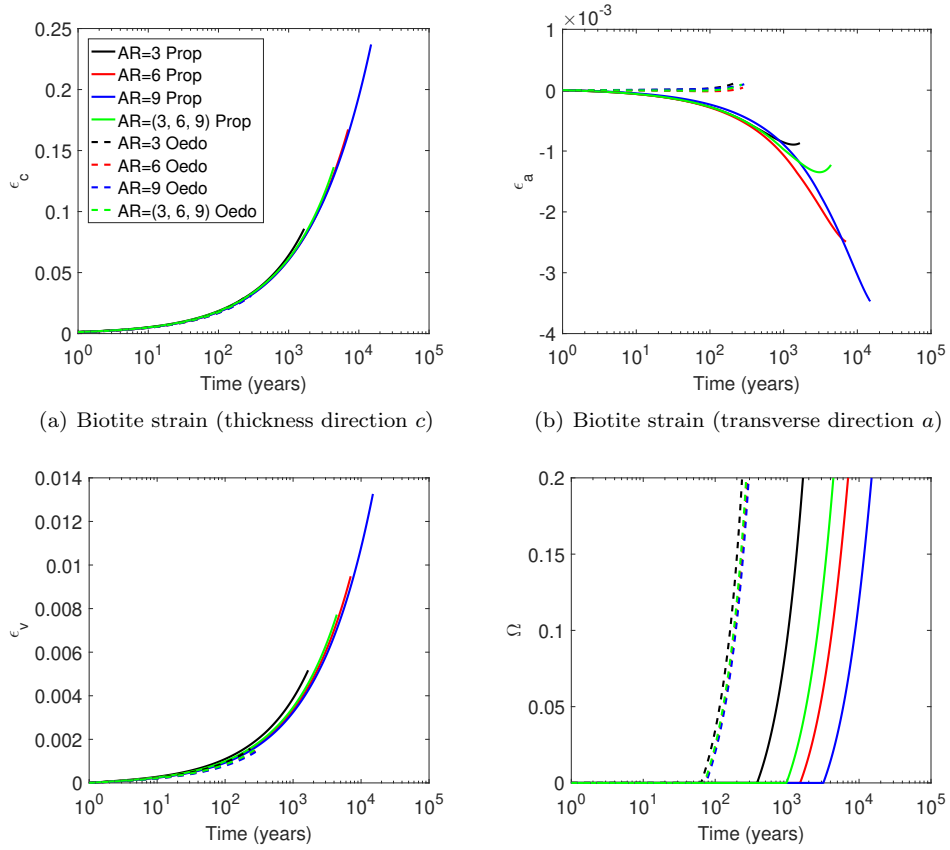

(a) Biotite strain (thickness direction c)

(b) Biotite strain (transverse direction a)

(c) Volumetric strain of bedrock REV

(d) Damage in the matrix

Figure B.2. Effect of biotite aspect ratio (AR) on strains and damage under proportional stress and oedometric boundary conditions. **a.** Biotite strain in the the thickness direction c (ϵ_c) shows negligible sensitivity to aspect ratio under both proportional stress and oedometric boundary conditions. **b.** Biotite strain in the transverse direction (ϵ_a) is close to 0 under oedometric boundary conditions. **c.** The REV volumetric strain (ϵ_v) exhibits minor sensitivity to aspect ratio under oedometric boundary conditions. **d.** Bedrock damage (Ω) exhibits negligible sensitivity to aspect ratio under oedometric boundary conditions. In each simulation, initial biotite abundance was 15%, the depth of bedrock was 10 m, the overburden density was $\rho = 2000$ kg m^{-3}, and the initial orientation of all biotite a-axes were 30° relative to the horizontal.

Acknowledgments

This research was supported by the U.S. National Science Foundation under grants EAR-1755321 ("Collaborative research: Microscopic fracturing and macroscopic weakening: A novel model for bedrock fracturing by biotite weathering") to Ferrier, Arson, and West, and 1552368 ("CAREER: Multiphysics Damage and Healing of Rocks for Performance Enhancement of Geo-Storage Systems - A Bottom-Up Research and Education Approach") to Arson.

List of Symbols

a	Long axes of the spheroidal mineral inclusions
$\mathbf{A}_i$	Concentration tensor of the component i
$\mathbf{A}_i^o$	Concentration tensor of the matrix component
α	Damage constitutive parameters
β	Damage constitutive parameters
c	Short axes of the spheroidal mineral inclusions
$\mathbf{C}_{hom}$	Homogenized stiffness of the REV
$\mathbf{C}_i$	Stiffness of the component i
$\mathbf{C}_o$	Stiffness of matrix
$\mathbf{D}_{ij}$	Influence tensor
δ_{ij}	Kronecker delta
ϵ_a	Total strain of inclusions in the direction of long axes
ϵ_c	Total strain of inclusions in the direction of short axes
ϵ_i	Local total strain of component i
ϵ_m	Strain field in the matrix
ϵ_a^c	Chemical strain of inclusions in the direction of long axes
ϵ_c^c	Chemical strain of inclusions in the direction of short axes
ϵ_i^c	Local chemical strain of component i
ϵ_v	Volumetric strain of the REV
$\bar{\epsilon}$	Strain of the REV
f_d	Damage criterion
ϕ_a	Volume fraction of component i
g	Gravitational acceleration
h	Depth of the bedrock
$\mathbf{I}$	Fourth-order identity tensor
k_0	Damage initiation threshold
k_1	Damage hardening parameter
K	Ratio between the horizontal and vertical stresses on the bedrock
λ	Lamé constants of the non-damaged matrix
μ	Lamé constants of the non-damaged matrix
n	Number of components in the REV
ν_m	Molar volume of weathered biotite
θ	Orientation of long axis from the horizontal
Q	Number of moles of weathered biotite in the REV
R	Weathering rate of biotite per unit mineral surface area
ρ	Density of bedrock
S	Total biotite surface area within the REV
σ_i	Local total stress of component i
σ_h	Lateral boundary stress applied on the bedrock
σ_v	Vertical stress applied on the bedrock
$\bar{\sigma}$	Stress of the REV
t	Weathering time
t_{tag}	Time until damage initiation
η_i	Chemical weathering strain of component i
$V_{mineral}$	Volume of unweathered mineral
$V_{mineral}^w$	Volume of weathered mineral

V_b	Volume of unweathered biotite
$V_{b,initial}$	Initial volume of biotite
V_b^w	Volume of weathered biotite
Y_d	Damage driving force
Ψ_s	Helmholtz free energy of the REV
Ω	Damage variable

References

Abidi, S., Joliff, Y., & Favotto, C. (2016). Impact of perlite, vermiculite and cement on the young modulus of a plaster composite material: Experimental, analytical and numerical approaches. *Composites Part B: Engineering*, *92*, 28 - 36. Retrieved from `http://www.sciencedirect.com/science/article/pii/S1359836816001487` doi: https://doi.org/10.1016/j.compositesb.2016.02.034

Ahn, J. H., & Peacor, D. R. (1987). Kaolinitization of biotite; TEM data and implications for an alteration mechanism. *American Mineralogist*, *72*(3-4), 353–356.

Anderson, R. S. (2002). Modeling the tor-dotted crests, bedrock edges, and parabolic profiles of high alpine surfaces of the wind river range, wyoming. *Geomorphology*, *46*(1-2), 35–58.

Anderson, S. P., Dietrich, W. E., & Brimhall Jr, G. H. (2002). Weathering profiles, mass-balance analysis, and rates of solute loss: Linkages between weathering and erosion in a small, steep catchment. *Geological Society of America Bulletin*, *114*(9), 1143–1158.

Banfield, J. F., & Eggleton, R. A. (1988). Transmission Electron Microscope Study of Biotite Weathering. *Clays and Clay Minerals*, *36*, 47-60. doi: 10.1346/CCMN.1988.0360107

Bateman, P. C. (1992). *Plutonism in the central part of the sierra nevada batholith, california* (Tech. Rep.).

Bažant, P., & Oh, B. (1986). Efficient numerical integration on the surface of a sphere. *ZAMM-Journal of Applied Mathematics and Mechanics/Zeitschrift für Angewandte Mathematik und Mechanik*, *66*(1), 37–49.

Berner, R. A., Lasaga, A. C., & Garrels, R. M. (1983). The carbonate-silicate geochemical cycle and its effect on atmospheric carbon dioxide over the past 100 million years. *American Journal of Science*, *283*(7), 641–683.

Bisdom, E., Stoops, G., Delvigne, J., Curmi, P., & Altemuller, H. (1982). Micromorphology of weathering biotite and its secondary products. *Pedologie*, *32*(2), 225–252.

Bosworth, W. (1981). Strain-induced preferential dissolution of halite. *Tectonophysics*, *78*(1-4), 509–525.

Brantut, N., Baud, P., Heap, M., & Meredith, P. (2012). Micromechanics of brittle creep in rocks. *Journal of Geophysical Research: Solid Earth*, *117*(B8).

Brantut, N., Heap, M., Meredith, P., & Baud, P. (2013). Time-dependent cracking and brittle creep in crustal rocks: A review. *Journal of Structural Geology*, *52*, 17–43.

Bray, A. W., Oelkers, E. H., Bonneville, S., Wolff-Boenisch, D., Potts, N. J., Fones, G., & Benning, L. G. (2015). The effect of ph, grain size, and organic ligands on biotite weathering rates. *Geochimica et Cosmochimica Acta*, *164*, 127–145.

Budiansky, B., & O'connell, R. J. (1976). Elastic moduli of a cracked solid. *International journal of Solids and structures*, *12*(2), 81–97.

Buss, H. L., Lara, M. C., Moore, O. W., Kurtz, A. C., Schulz, M. S., & White, A. F. (2017). Lithological influences on contemporary and long-term regolith weathering at the Luquillo Critical Zone Observatory. *Geochimica et Cosmochimica Acta*, *196*, 224–251.

Buss, H. L., Sak, P. B., Webb, S. M., & Brantley, S. L. (2008). Weathering of the Rio Blanco quartz diorite, Luquillo Mountains, Puerto Rico: Coupling

oxidation, dissolution, and fracturing. *Geochimica et Cosmochimica Acta*, *72*(18), 4488 - 4507. Retrieved from `http://www.sciencedirect.com/science/article/pii/S0016703708003955` doi: https://doi.org/10.1016/j.gca.2008.06.020

da Fonseca, A., & e Sousa, J. (2001). At rest coefficient of earth pressure in saprolitic soils from granite. In *Proceedings of the international conference on soil mechanics and geotechnical engineering* (Vol. 1, pp. 397–400).

Dixon, J. L., Heimsath, A. M., & Amundson, R. (2009). The critical role of climate and saprolite weathering in landscape evolution. *Earth Surface Processes and Landforms*, *34*(11), 1507–1521.

Dong, H., Peacor, D. R., & Murphy, S. F. (1998). Tem study of progressive alteration of igneous biotite to kaolinite throughout a weathered soil profile. *Geochimica et Cosmochimica Acta*, *62*(11), 1881 - 1887. Retrieved from `http://www.sciencedirect.com/science/article/pii/S0016703798000969` doi: https://doi.org/10.1016/S0016-7037(98)00096-9

Eppes, M.-C., & Keanini, R. (2017). Mechanical weathering and rock erosion by climate-dependent subcritical cracking. *Reviews of Geophysics*, *55*(2), 470–508.

Eshelby, J. D. (1957). The determination of the elastic field of an ellipsoidal inclusion, and related problems. *Proceedings of the Royal Society of London A: Mathematical, Physical and Engineering Sciences*, *241*(1226), 376–396. Retrieved from `http://rspa.royalsocietypublishing.org/content/241/1226/376` doi: 10.1098/rspa.1957.0133

Fanning, D. S., Keramidas, V. Z., & El-Desoky, M. A. (1989). Micas. *Minerals in soil environments*(mineralsinsoile), 551–634.

Ferrier, K. L., Kirchner, J. W., & Finkel, R. C. (2012). Weak influences of climate and mineral supply rates on chemical erosion rates: Measurements along two altitudinal transects in the idaho batholith. *Journal of Geophysical Research: Earth Surface*, *117*(F2).

Ferrier, K. L., Kirchner, J. W., Riebe, C. S., & Finkel, R. C. (2010). Mineral-specific chemical weathering rates over millennial timescales: measurements at rio icacos, puerto rico. *Chemical Geology*, *277*(1-2), 101–114.

Fletcher, R., Buss, H., & Brantley, S. (2006). A spheroidal weathering model coupling porewater chemistry to soil thicknesses during steady-state denudation. *Earth and Planetary Science Letters*, *244*(1-2), 444–457.

Germanovich, L., Salganik, R., Dyskin, A., & Lee, K. (1994). Mechanisms of brittle fracture of rock with pre-existing cracks in compression. *Pure and Applied Geophysics*, *143*(1-3), 117–149.

Goodfellow, B. W., Hilley, G. E., Webb, S. M., Sklar, L. S., Moon, S., & Olson, C. A. (2016). The chemical, mechanical, and hydrological evolution of weathering granitoid. *Journal of Geophysical Research: Earth Surface*, *121*(8), 1410–1435.

Grant, W. H. (1962). Weathering of stone mountain granite. *Clays and clay minerals*, *11*, 65–73.

Grgic, D., Giraud, A., & Auvray, C. (2013). Impact of chemical weathering on micro/macro-mechanical properties of oolithic iron ore. *International Journal of Rock Mechanics and Mining Sciences*, *64*, 236–245.

Griffiths, L., Heap, M., Baud, P., & Schmittbuhl, J. (2017). Quantification of microcrack characteristics and implications for stiffness and strength of granite. *International Journal of Rock Mechanics and Mining Sciences*, *100*, 138–150.

Guéry, A. A.-C., Cormery, F., Shao, J.-F., & Kondo, D. (2008). A micromechanical model of elastoplastic and damage behavior of a cohesive geomaterial. *International Journal of Solids and structures*, *45*(5), 1406–1429.

Halm, D., & Dragon, A. (1998). An anisotropic model of damage and frictional sliding for brittle materials. *European Journal of Mechanics - A/Solids*,

17(3), 439 - 460. Retrieved from http://www.sciencedirect.com/science/article/pii/S0997753898800545 doi: https://doi.org/10.1016/S0997-7538(98)80054-5

Halm, D., & Dragon, A. (2002). Modélisation de l'endommagement par mésofissuration du granite. *Revue française de génie civil*, *6*(1), 21–33.

Heimsath, A. M., Chappell, J., Dietrich, W. E., Nishiizumi, K., & Finkel, R. C. (2001). Late quaternary erosion in southeastern australia: a field example using cosmogenic nuclides. *Quaternary International*, *83*, 169–185.

Hellmann, R., & Tisserand, D. (2006). Dissolution kinetics as a function of the gibbs free energy of reaction: An experimental study based on albite feldspar. *Geochimica et Cosmochimica Acta*, *70*(2), 364–383.

Hill, R. (1965). Continuum micro-mechanics of elastoplastic polycrystals. *Journal of the Mechanics and Physics of Solids*, *13*(2), 89 - 101. Retrieved from http://www.sciencedirect.com/science/article/pii/0022509665900232 doi: http://dx.doi.org/10.1016/0022-5096(65)90023-2

Houlsby, G. T., & Puzrin, A. M. (2007). *Principles of hyperplasticity: an approach to plasticity theory based on thermodynamic principles*. Springer Science & Business Media.

Hu, D., Zhou, H., Hu, Q., Shao, J., Feng, X., & Xiao, H. (2012). A hydro-mechanical-chemical coupling model for geomaterial with both mechanical and chemical damages considered. *Acta Mechanica Solida Sinica*, *25*(4), 361–376.

Jin, W., Xu, H., Arson, C., & Busetti, S. (2017). Computational model coupling mode ii discrete fracture propagation with continuum damage zone evolution. *International Journal for Numerical and Analytical Methods in Geomechanics*, *41*(2), 223–250.

Köhler, S. J., Dufaud, F., & Oelkers, E. H. (2003). An experimental study of illite dissolution kinetics as a function of ph from 1.4 to 12.4 and temperature from 5 to 50 c. *Geochimica et Cosmochimica Acta*, *67*(19), 3583–3594.

Lacerda, W. A. (2007). Landslide initiation in saprolite and colluvium in southern Brazil: field and laboratory observations. *Geomorphology*, *87*(3), 104–119.

Lemaitre, J., & Desmorat, R. (2005). *Engineering damage mechanics: ductile, creep, fatigue and brittle failures*. Springer Science & Business Media.

Levin, V. M. (1967). Thermal expansion coefficient of heterogeneous materials. *Mekhanika Tverdogo Tela*, *2*(1), 83-94.

Li, L., Tang, C., Wang, S., & Yu, J. (2013). A coupled thermo-hydrologic-mechanical damage model and associated application in a stability analysis on a rock pillar. *Tunnelling and Underground Space Technology*, *34*, 38–53.

Maher, K. (2010). The dependence of chemical weathering rates on fluid residence time. *Earth and Planetary Science Letters*, *294*(1-2), 101–110.

Maher, K., DePaolo, D. J., & Christensen, J. N. (2006). U–sr isotopic speedometer: fluid flow and chemical weathering rates in aquifers. *Geochimica et Cosmochimica Acta*, *70*(17), 4417–4435.

Maher, K., Steefel, C. I., White, A. F., & Stonestrom, D. A. (2009). The role of reaction affinity and secondary minerals in regulating chemical weathering rates at the santa cruz soil chronosequence, california. *Geochimica et Cosmochimica Acta*, *73*(10), 2804–2831.

McFadden, L., Eppes, M., Gillespie, A., & Hallet, B. (2005). Physical weathering in arid landscapes due to diurnal variation in the direction of solar heating. *Geological Society of America Bulletin*, *117*(1-2), 161–173.

Miller, D. J., & Dunne, T. (1996). Topographic perturbations of regional stresses and consequent bedrock fracturing. *Journal of Geophysical Research: Solid Earth*, *101*(B11), 25523–25536.

Moon, S., Perron, J., Martel, S., Holbrook, W., & St. Clair, J. (2017). A model of three-dimensional topographic stresses with implications for bedrock fractures, surface processes, and landscape evolution. *Journal of Geophysical Research:*

Earth Surface, *122*(4), 823–846.

Moos, D., Dvorkin, J., & Hooks, A. J. (1997). Application of theoretically derived rock physics relationships for clastic rocks to log data from the wilmington field, CA. *Geophysical Research Letters*, *24*(3), 329-332. Retrieved from `https://agupubs.onlinelibrary.wiley.com/doi/abs/10.1029/96GL02392` doi: 10.1029/96GL02392

Mori, T., & Tanaka, K. (1973). Average stress in matrix and average elastic energy of materials with misfitting inclusions. *Acta Metallurgica*, *21*(5), 571 - 574. Retrieved from `http://www.sciencedirect.com/science/article/pii/0001616073900643` doi: https://doi.org/10.1016/0001-6160(73)90064-3

Mura, T. (1987). Micromechanics of defects in solids (martinus nijhoff, dordrecht, 1987). *Google Scholar*, 1.

Murphy, S. F., Brantley, S. L., Blum, A. E., White, A. F., & Dong, H. (1998). Chemical weathering in a tropical watershed, Luquillo Mountains, Puerto Rico: Ii. Rate and mechanism of biotite weathering. *Geochimica et Cosmochimica Acta*, *62*(2), 227–243.

Navarre-Sitchler, A., Brantley, S. L., & Rother, G. (2015). How porosity increases during incipient weathering of crystalline silicate rocks. *Reviews in Mineralogy and Geochemistry*, *80*(1), 331–354.

Navarre-Sitchler, A., Steefel, C. I., Sak, P. B., & Brantley, S. L. (2011). A reactive-transport model for weathering rind formation on basalt. *Geochimica et Cosmochimica Acta*, *75*(23), 7644–7667.

Navarre-Sitchler, A. K., Cole, D. R., Rother, G., Jin, L., Buss, H. L., & Brantley, S. L. (2013). Porosity and surface area evolution during weathering of two igneous rocks. *Geochimica et Cosmochimica Acta*, *109*, 400–413.

Perillo, C., Gupta, S., Nater, E., & Moncrief, J. (1999). Prevalence and initiation of preferential flow paths in a sandy loam with argillic horizon. *Geoderma*, *89*(3-4), 307–331.

Pichler, B., & Hellmich, C. (2010). Estimation of influence tensors for eigenstressed multiphase elastic media with nonaligned inclusion phases of arbitrary ellipsoidal shape. *Journal of engineering mechanics*, *136*(8), 1043–1053.

Poulet, T., Karrech, A., Regenauer-Lieb, K., Fisher, L., & Schaubs, P. (2012). Thermal–hydraulic–mechanical–chemical coupling with damage mechanics using ESCRIPTRT and ABAQUS. *Tectonophysics*, *526*, 124–132.

Reis, F. D. A., & Brantley, S. L. (2017). Models of transport and reaction describing weathering of fractured rock with mobile and immobile water. *Journal of Geophysical Research: Earth Surface*, *122*(3), 735–757.

Rempe, D. M., & Dietrich, W. E. (2014). A bottom-up control on fresh-bedrock topography under landscapes. *Proceedings of the National Academy of Sciences*, *111*(18), 6576–6581.

Schoenball, M., Sahara, D. P., & Kohl, T. (2014). Time-dependent brittle creep as a mechanism for time-delayed wellbore failure. *International Journal of Rock Mechanics and Mining Sciences*, *70*, 400–406.

Shen, X., & Arson, C. (2019). An isotropic self-consistent homogenization scheme for chemo-mechanical healing driven by pressure solution in halite. *International Journal of Solids and Structures*, *161*, 96–110.

Shiels, A. B., & Walker, L. R. (2003). Bird perches increase forest seeds on Puerto Rican landslides. *Restoration Ecology*, *11*(4), 457–465.

Slim, M., Perron, J. T., Martel, S. J., & Singha, K. (2015). Topographic stress and rock fracture: a two-dimensional numerical model for arbitrary topography and preliminary comparison with borehole observations. *Earth Surface Processes and Landforms*, *40*(4), 512–529.

St. Clair, J., Moon, S., Holbrook, W., Perron, J., Riebe, C., Martel, S., ... others (2015). Geophysical imaging reveals topographic stress control of bedrock weathering. *Science*, *350*(6260), 534–538.

Steefel, C. I., & Maher, K. (2009). Fluid-rock interaction: A reactive transport approach. *Reviews in mineralogy and geochemistry*, *70*(1), 485–532.

Stefanou, I., & Sulem, J. (2014). Chemically induced compaction bands: Triggering conditions and band thickness. *Journal of Geophysical Research: Solid Earth*, *119*, 880–899.

Takaya, Y., Hatta, T., & Matsukura, Y. (2014, 07). Differential roles of plagioclase and biotite in the early stage weathering of granite: a solid-sided approach combining laboratory experiment and surface analysis. *Zeitschrift für Geomorphologie*, *58*(2), 233-249. Retrieved from `http://dx.doi.org/10.1127/0372-8854/2014/0123` doi: 10.1127/0372-8854/2014/0123

Voyiadjis, G. Z., & Kattan, P. I. (2005). *Damage mechanics*. CRC Press.

Wahrhaftig, C. (1965). Stepped topography of the southern Sierra Nevada, California. *Geological Society of America Bulletin*, *76*(10), 1165–1190.

Walker, J. C., Hays, P., & Kasting, J. F. (1981). A negative feedback mechanism for the long-term stabilization of earth's surface temperature. *Journal of Geophysical Research: Oceans*, *86*(C10), 9776–9782.

West, A. J. (2012). Thickness of the chemical weathering zone and implications for erosional and climatic drivers of weathering and for carbon-cycle feedbacks. *Geology*, *40*(9), 811–814.

White, A. F., Blum, A. E., Schulz, M. S., Huntington, T. G., Peters, N. E., & Stonestrom, D. A. (2002). Chemical weathering of the panola granite: Solute and regolith elemental fluxes and the weathering rate of biotite. *Water rock interaction, ore deposits, and environmental geochemistry, a tribute to David A. Crerar: Geochemical Society Special Publication*, *7*, 37–59.

White, A. F., & Brantley, S. L. (2003). The effect of time on the weathering of silicate minerals: why do weathering rates differ in the laboratory and field? *Chemical Geology*, *202*(3), 479 - 506. Retrieved from `http://www.sciencedirect.com/science/article/pii/S0009254103002560` (Controls on Chemical Weathering) doi: https://doi.org/10.1016/j.chemgeo.2003.03.001

White, A. F., Schulz, M. S., Vivit, D. V., Blum, A. E., Stonestrom, D. A., & Anderson, S. P. (2008). Chemical weathering of a marine terrace chronosequence, santa cruz, california i: interpreting rates and controls based on soil concentration–depth profiles. *Geochimica et Cosmochimica Acta*, *72*(1), 36–68.

Yasuhara, H., Kinoshita, N., Ohfuji, H., Lee, D. S., Nakashima, S., & Kishida, K. (2011). Temporal alteration of fracture permeability in granite under hydrothermal conditions and its interpretation by coupled chemo-mechanical model. *Applied Geochemistry*, *26*(12), 2074–2088.

Yu, H.-S. (2007). *Plasticity and geotechnics* (Vol. 13). Springer Science & Business Media.